

RESEARCH ARTICLE

10.1002/2015JF003663

Key Points:

- Variations in erosion rate with time scale reveal the importance of wildfire
- Post-wildfire erosion is >90% of all erosion in Valles Caldera
- Future increases in wildfire area and severity may affect landscape denudation

Correspondence to:

J. D. Pelletier,
jdpellet@email.arizona.edu

Citation:

Orem, C. A., and J. D. Pelletier (2016), The predominance of post-wildfire erosion in the long-term denudation of the Valles Caldera, New Mexico, *J. Geophys. Res. Earth Surf.*, *121*, 843–864, doi:10.1002/2015JF003663.

Received 6 JUL 2015

Accepted 18 MAR 2016

Accepted article online 30 MAR 2016

Published online 3 MAY 2016

The predominance of post-wildfire erosion in the long-term denudation of the Valles Caldera, New Mexico

Caitlin A. Orem¹ and Jon D. Pelletier¹¹Department of Geosciences, University of Arizona, Tucson, Arizona, USA

Abstract Wildfires can dramatically increase erosion rates over time scales on the order of several years, yet few data firmly constrain the relative importance of post-wildfire erosion in the long-term denudation of landscapes. We tested the hypothesis that wildfire-affected erosion is responsible for a large majority of long-term denudation in the uplands of the Valles Caldera, New Mexico, by quantifying erosion rates in wildfire-affected and non-wildfire-affected watersheds over short ($\sim 10^0$ – 10^1 years) time scales using suspended sediment loads, multitemporal terrestrial laser scanning, and airborne laser scanning and over long ($\sim 10^3$ – 10^6 years) time scales using ^{10}Be inventories and incision into a dated paleosurface. We found that following the Las Conchas fire in 2011, mean watershed-averaged erosion rates were more than $1000 \mu\text{m yr}^{-1}$, i.e., $\sim 10^3$ – 10^5 times higher than nearby unburned watersheds of similar area, relief, and lithology. Long-term denudation rates are on the order of 10 – $100 \mu\text{m yr}^{-1}$. Combining data for wildfire-affected and non-wildfire-affected erosion rates into a long-term denudation rate budget, we found that wildfire-affected erosion is responsible for at least 90% of denudation over geologic time scales in our study area despite the fact that such conditions occur only at a small fraction of the time. Monte Carlo analyses demonstrate that this conclusion is robust with respect to uncertainties in the rates and time scales used in the calculations.

1. Introduction

The loss of vegetation cover and changes to soil characteristics associated with wildfires triggers an increase in erosion rates following high-severity wildfires [e.g., Fowler, 1979; Swanson, 1981; Wagenbrenner and Robichaud, 2014]. Many factors control the magnitude and duration of the increase in erosion rate above non-wildfire-affected conditions, including the extent and severity of wildfire (which, in turn, controls the degree of vegetation loss and the change of soil characteristics, the timing and magnitude of post-wildfire runoff events, the steepness of the landscape, and the time scale of recovery of vegetative cover after wildfires). Studies of fire-related alluvial fan sedimentation records suggest that wildfire-affected erosion may, in some locations, be responsible for the majority of denudation over Holocene time scales [e.g., Pierce *et al.*, 2004] despite the fact that wildfire-affected erosion occurs only a small fraction of the time, e.g., on the order of a few years following high-severity wildfires that may occur once every few centuries.

Alluvial fan sedimentation records may overestimate or underestimate the relative importance of wildfire, however. As Meyer *et al.* [1995] noted, “The actual percentage of alluvial fan sediment produced because of fire may be greater, because most streamflow and hyperconcentrated-flow deposits retain no diagnostic evidence of origin in burned basins, and subsequent dilute flood flows may rework fire-related debris flow sediments. Conversely, sampling may have been somewhat biased toward a greater proportion of fire-related sediments, as data were often collected at exposures where such deposits were least ambiguous for dating purposes.” Similarly, Fitch and Meyer [2013] pointed out that an increase in wildfire-affected erosion can lead to a decrease in wildfire-affected sedimentation on alluvial fans if the increase in erosion leads to fan incision and bypassing of sediment to incised channels farther downstream.

Here we take an alternative approach to quantifying the relative importance of wildfire-affected erosion over geologic time scales that is based on independent measurements of long-term denudation rates, short-term erosion rates under wildfire-affected and non-wildfire-affected conditions, and the recovery time over which erosion rates return to non-wildfire-affected levels. Our analysis predicts the recurrence interval (RI) required to close the denudation rate budget, i.e., the recurrence interval required for the cumulative impact of wildfire-affected and non-wildfire-affected erosion to match the measured long-term denudation rate. The RI value required to close the denudation rate budget is then compared to independent constraints obtained from proxies for high-severity wildfires. As the frequency of large, high-severity wildfires increases in the

western U.S. [Westerling *et al.*, 2006; Miller *et al.*, 2009; Williams *et al.*, 2013], it is crucial that the geomorphic effects of wildfire be quantified on both the short-term, human, and geologic time scales.

The relative importance of frequent, small versus rare, large erosional events in driving the long-term denudation of landscapes is still a fundamental question in geomorphology [Wolman and Gerson, 1978]. To address this question, Kirchner *et al.* [2001] quantified sediment yields over time scales of $\sim 10^1$ years by analyzing suspended sediment loads, $\sim 10^3$ – 10^4 years using ^{10}Be inventories, and $\sim 10^6$ years using apatite fission track in mountainous, conifer-forested areas of central Idaho. These authors found that erosion rates over short time scales ($\sim 10^1$ years) were significantly lower than long-term rates. Kirchner *et al.* [2001] suggested that the short-term rates did not usually incorporate the rare, large erosional events that are responsible for the majority of denudation over geologic time scales (i.e., $> 10^3$ years). Kirchner *et al.* [2001] associated these geomorphically most effective events with intense rainstorms but also suggested that they could be associated with disturbance events, principally wildfires, which alter land cover and soil hydrologic conductivity. Subsequent post-wildfire erosion studies in central Idaho proposed that episodic post-wildfire debris flows could explain the difference between high, long-term and relatively low, short-term erosion rates [Meyer *et al.*, 2001].

All of the erosion rate data we present are based on the volume of sediment leaving a watershed of a given contributing area per unit time. As such, they are watershed-averaged erosion rates. Erosion may be localized within the watersheds; the reporting of an average rate does not imply uniformity of erosion rates within the watershed. We use the term denudation rate to refer to the long-term wearing away of the landscape that results from the cumulative effects of short-term erosional processes that export sediment from the 1.3–13 km² watersheds we studied. Erosion rates we present are the mean physical erosion rates for a given watershed. Chemical erosion rates are also calculated and were used to adjust the measured total erosion rate for the effects of chemical erosion and to demonstrate that the vast majority of total erosion occurs by physical processes, i.e., sediment transport, in the study area.

2. Study Area

The Valles Caldera formed circa 1.25 Ma in north central New Mexico as part of the Jemez Mountains volcanic field [Goff *et al.*, 2006a]. The caldera includes Redondo Mountain, a resurgent dome composed predominantly of the Tshirge member of the Bandelier tuff and several smaller rhyolitic domes that erupted along the caldera ring fracture between circa 1.2 Ma and 0.5 Ma [Goff *et al.*, 2006a, 2006b; Phillips *et al.*, 2007]. More recent eruptions occurred along the southern portion of the ring fracture between 60 and 37 ka [Toyoda *et al.*, 1995; Goff *et al.*, 2006a]. Elevation above sea level in the Valles Caldera varies from approximately 2500 m in the lowest meadows to 3430 m at the summit of Redondo Mountain.

Our study watersheds are of similar contributing area, geology, and relief and are located on two resurgent domes (Redondo Mountain and Cerro del Medio) dated to approximately 1.24 and 1.22 Ma, respectively [Phillips *et al.*, 2007] (Figure 1). Average slopes in the two watersheds on Cerro del Medio are 14.7° and 16.1°, respectively, while average slopes for the watersheds on Redondo Mountain range from 13.3° to 20.1°.

The modern climate in the Valles Caldera is subhumid continental. Approximately half of the annual precipitation falls during convective monsoonal storms during the summer months and the other half falls as snow in the winter [Muldavine and Tonne, 2003]. The largest historical stream discharges are recorded during periods of snowmelt in April and May. Average daily high temperatures vary from approximately 27°C in the summer to 4°C in the winter at nearby Los Alamos, NM [Muldavine and Tonne, 2003] (2231 m above sea level (asl)). Average annual precipitation is approximately 46.7 cm at nearby Los Alamos, but it is estimated that this value increases to approximately 90 cm at the rim of the Valles Caldera [Muldavine and Tonne, 2003].

The modern vegetation of the Valles Caldera varies with elevation. Grasslands at the lowest elevations are composed of sedges, grasses, and forbs [Muldavine and Tonne, 2003]. Forest types include spruce and fir at the highest elevations, mixed-conifer forest and woodlands at intermediate elevations, and ponderosa pine forests at lower elevations [Muldavine and Tonne, 2003]. The soils within the Valles Caldera range from Andisols, Alfisols, and Inceptisols of variable thickness in the uplands to deep Mollisols in the valleys [Muldavine and Tonne, 2003]. The texture of the upland soils is predominantly coarse sandy loam [U.S. Department of Agriculture, 2008].

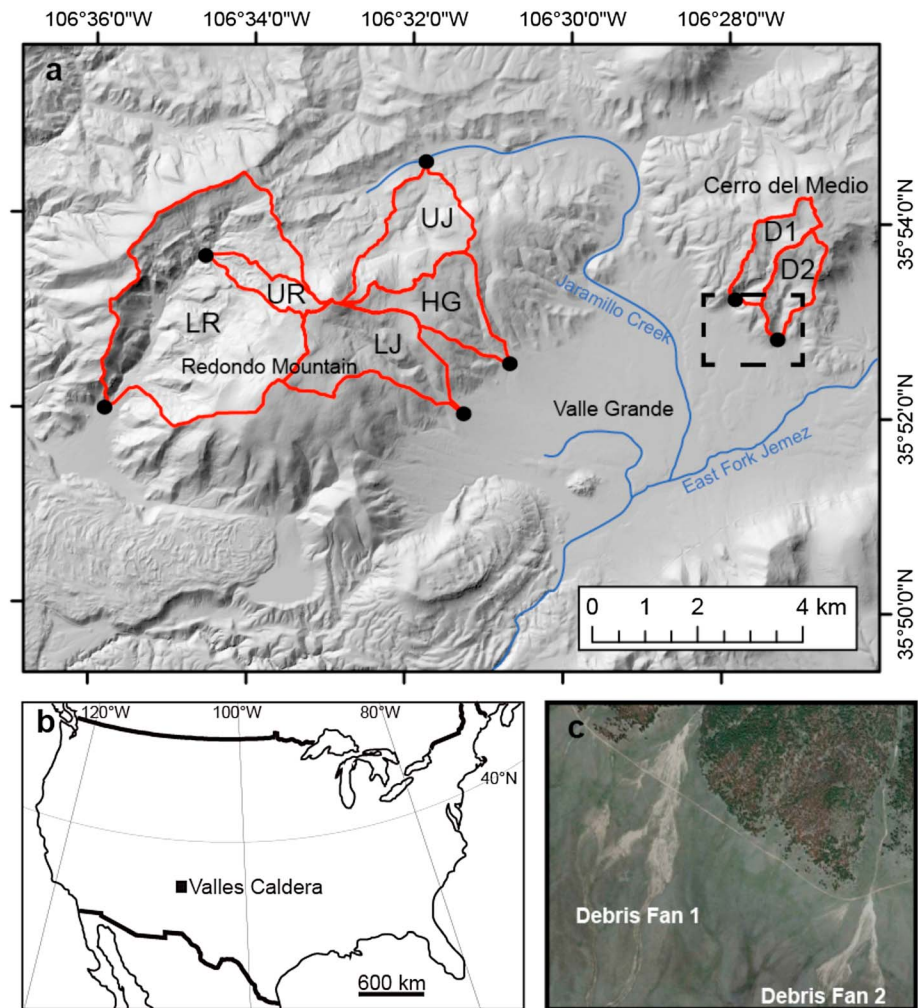


Figure 1. (a) Map of the Valles Caldera, NM, with sample locations (black circles) and study watersheds (red outline) shown. All study watersheds are shown: History Grove (HG), La Jara (LJ), Upper Jaramillo (UJ), Upper Redondo (UR), Lower Redondo (LR), Debris 1 (D1), and Debris 2 (D2). (b) Map showing the location of the Valles Caldera. (c) Aerial photograph of the post-wildfire deposits on the two piedmont surfaces located below the D1 and D2 watersheds (coverage area of Figure 1c shown as dashed rectangle in Figure 1a).

Sediment cores from the Chihuahueros and Alamo bogs of the Jemez Mountains provide a record of the climatic and vegetation shifts from approximately 15,000 cal years B.P. to the midtwentieth century in the study area [Anderson *et al.*, 2008]. During the late glacial period, the record indicates that tundra or steppe vegetation was present. Remains of tree species are prevalent in the bog beginning at 14,000 cal years B.P., coincident with warming during the Pleistocene-to-Holocene transition. Only minor shifts in tree species composition were recorded in the bog records during the Holocene, indicating that a mixed-conifer forest was dominant over this time interval. The driest period in the Holocene occurred from 8500 to 6400 cal years B.P. Higher charcoal input rates were recorded after 6400 cal years B.P., suggesting higher biomass production rates from 6400 cal years B.P. to the present compared to the earlier dry interval.

In the summer of 2011 the Las Conchas fire burned approximately 630 km² of the eastern portion of the Valles Caldera and the adjacent Parajito Plateau. This study focuses only on the portion of the burned area within the caldera (approximately 150 km²) where we have paired burned and unburned watersheds of similar area, relief, and lithology. Following the Las Conchas fire, storms of moderate intensity and duration triggered large debris-laden flows in the two wildfire-affected watersheds we monitored (D1 and D2, Figure 1). The largest rainstorm occurred on 3 August 2011, during which rain gages and Next Generation Radar recorded a storm with a maximum 1 h intensity of 33 mm (equivalent to a 5 years recurrence interval

event) over the two wildfire-affected watersheds [Orem and Pelletier, 2015]. Field observations indicate that sediment entrained into these debris-laden flows was sourced from both hillslope (rilling, gullying, and evidence for sediment transport by overland flow were observed) and hollow and valley bottom (gullying) locations within the watersheds. Orem and Pelletier [2015] monitored the sediment delivery from D1 and D2 to their adjacent piedmonts using multitemporal lidar and found that each subsequent rainstorm deposited less sediment volume than the previous event over a 2 year period.

A key assumption of our analysis is that long-runout debris-laden flows (i.e., debris-laden flows that export sediment from watersheds greater than or equal to $\sim 1 \text{ km}^2$ in area) are rare in the absence of wildfire in the study area. This assumption provides a basis for using suspended sediment loads from floods as a measure of erosion rates in non-wildfire-affected watersheds. Two lines of evidence support this assumption. First, there are no modern examples of debris-laden flow deposits on piedmonts within the Valles Caldera in the absence of wildfire. We examined Google Earth imagery from 2010 in addition to aerial photos acquired by the U.S. Soil Conservation Service in 1935 (obtained from <http://rgis.unm.edu/getdata/>) for all of the depositional piedmonts of the Valles Caldera and found no visible debris-laden flow deposits on piedmonts. Such cases would have been visually apparent had they exceeded $\sim 1000 \text{ m}^2$ in area since the piedmonts of the Valles Caldera are uniformly grass covered and unchanneled except for the recent deposits associated with the Las Conchas (2011) and Thompson Ridge (2013) fires, which stand out in aerial imagery due to the contrast in color and texture between grass and debris-laden flow deposits. Second, where bulking-type debris flows have been documented in undisturbed areas of the western U.S., they tend to occur in areas that are steeper and/or have more bare ground than our study area. As Costa [1984] noted, "prerequisite conditions for most debris flows include an abundant source of unconsolidated fine-grained rock and soil debris, steep slopes, a large but intermittent source of moisture, and sparse vegetation." Vegetation in the Valles Caldera uniformly covers hillslopes in the absence of wildfire, i.e., areas mapped as sparsely vegetated are limited to 0.18% of the area, not including the felsenmeer rock fields on the north and west sides of Redondo Mountain (1.03% of the study area) that are limited to the upper segments of hillslopes [Muldavin et al., 2006]. In their study of over 900 debris flows in burned and unburned watersheds of the western U.S., Canada, and Italy, Santi and Morandi [2013] found median gradients of channels that transported debris flows to be in the range of 28% to 90%, i.e., much higher than the slopes of 15% or less that characterize the channels of the Valles Caldera with contributing areas greater than $\sim 0.1 \text{ km}^2$ (see Pelletier and Orem [2014, Figure 8] for a slope-area plot). All of the debris flows triggered by the extreme September 2013 rainstorms in the Colorado Front Range occurred on slopes between 26° and 43° , with 78% of the events triggered on south facing slopes, which tend to have less vegetation cover than north facing slopes within the elevation range where the debris flows occurred (1600–2600 masl). In the Valles Caldera, slopes steeper than 30° are limited to 10% of upland areas (defined as $>5\%$ in slope). Debris-laden flows have certainly occurred on such steep slopes in the absence of wildfire, but the localized nature of these steep slopes combined with the relatively gentle gradients of channels in the Valles Caldera suggests that such flows were probably not of the long-runout type necessary to export sediment from watersheds larger than $\sim 1 \text{ km}^2$ in area. In the absence of long runouts, debris flows that occur within watersheds $\sim 1\text{--}10 \text{ km}^2$ in area simply redistribute mass within watersheds without resulting in any net erosion of the watershed because areas of erosion are balanced by areas of deposition.

3. Methods

3.1. Short-Term Erosion Rates and Recovery Times in Wildfire-Affected Watersheds From Airborne Laser Scanning and Terrestrial Laser Scanning

We differenced terrestrial laser scanning (TLS)-derived digital elevation models (DEMs) acquired using a Leica C10 ScanStation to measure the volumes of sediment deposited on the two piedmont surfaces we studied as a function of time following the Las Conchas fire. These data were used to calculate short-term ($\sim 10^0$ years) erosion rates and recovery times in the two wildfire-affected watersheds upstream from those piedmonts. TLS surveys of the piedmonts enabled us to quantify nearly all of the sediment exported from the watersheds since the piedmonts are nearly a closed depositional system (see section 5.1 for further discussion of this point). The decline in sediment yield through time can be fit to an exponential function to determine a recovery time. Because we did not have a prewildfire TLS-derived DEM, we used an airborne laser scanning

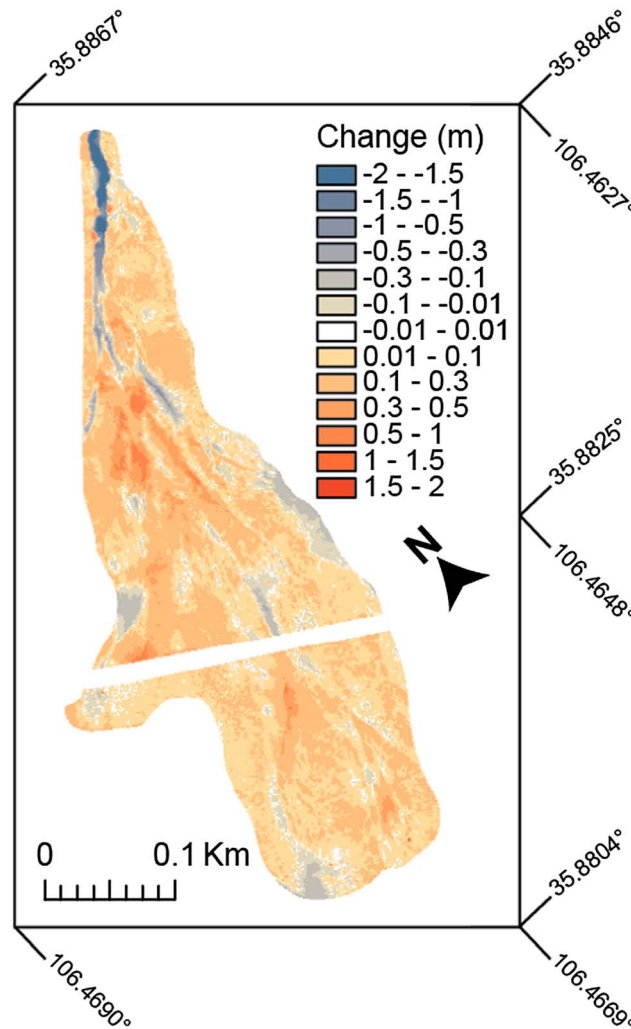


Figure 2. DEM of difference (raster showing the change in the surface between two TLS surveys) calculated for D1 that was used to calculate the volume of the sediment deposited on the surface and the erosion rate of the watershed.

the sediment exported from D1 and D2. *Pelletier and Orem* [2014] measured erosion rates in the year following the Las Conchas fire everywhere over an area of 186 km² using repeat ALS. *Pelletier and Orem* [2014] documented an average erosion rate of approximately 10³ μm yr⁻¹ (their Figures 11 and 12), with higher values (i.e., 10⁴–10⁵ μm yr⁻¹) associated with areas of high burn severity and/or especially steep topography. There is considerable uncertainty in values based on ALS change detection, however, given the fact that amounts of erosion or deposition less than 0.3 m cannot be firmly detected.

Table 1. TLS- and ALS-Derived Volume Change and Erosion Rates for the Two Watersheds We Monitored, i.e., Debris 1 (D1) and Debris 2 (D2)

Watershed	Volume Change (m ³)	Erosion Rate (μm yr ⁻¹) ^a
TLS Debris 1	11,036 ± 3,773	12,000 ± 4,100
TLS Debris 2	589 ± 145	660 ± 160
ALS Debris 1	10,976 ± 5,488	23,000 ± 1,000
ALS Debris 2	5,360 ± 2,680	12,000 ± 500

^aErrors given are propagated DEM error for TLS-derived erosion rates and ALS-derived erosion rates [*Orem and Pelletier*, 2015].

(ALS)-derived DEM from May 2010 as our prewildfire topography. As an alternative, we also estimated the prewildfire topography by interpolating among grass-covered portions of the first post-wildfire TLS-derived DEM (appropriate because points covered by grass did not undergo significant erosion or deposition between the fire event and the time of the first post-wildfire TLS survey in August 2011). We describe the data set and processing procedures briefly here. Additional details are provided in *Orem and Pelletier* [2015].

TLS surveys were conducted on the two piedmonts in August 2011, June 2012, September 2012, and May 2013. TLS data were collected on these dates to coincide with the end of the monsoon summer precipitation season in August–September and the end of the spring snowmelt season in May–June. Therefore, the TLS surveys are capturing surface change that occurred during the two major runoff seasons following the Las Conchas fire. TLS surveys of the Debris 1 (D1) and Debris 2 (D2) piedmonts (locations shown in Figure 1) included 10 and 20 scan positions and 4 and 13 georeferenced control points, respectively, resulting in a maximum distance of 50 m between scan stations. The point cloud densities were a minimum of 100 returns m⁻² everywhere within all eight surveys.

ALS surveys of the areas within the caldera burned by the Las Conchas fire complemented the TLS surveys of the

measured erosion rates in the year following the Las Conchas fire everywhere over an area of 186 km² using repeat ALS. *Pelletier and Orem* [2014] documented an average erosion rate of approximately 10³ μm yr⁻¹ (their Figures 11 and 12), with higher values (i.e., 10⁴–10⁵ μm yr⁻¹) associated with areas of high burn severity and/or especially steep topography. There is considerable uncertainty in values based on ALS change detection, however, given the fact that amounts of erosion or deposition less than 0.3 m cannot be firmly detected.

All TLS- and ALS-derived DEMs were differenced using ArcGIS and MATLAB software to create a DEM of difference (example shown in Figure 2). Total volume change was calculated by multiplying the sum of all vertical changes by the pixel area (Table 1). For DEMs derived from TLS data, no vertical change less than the combined error associated with each cell was used. DEMs derived from ALS data for the upland watersheds were further filtered

to remove change <0.3 m, change measured on slopes $>45^\circ$, and change measured on hillslopes with <1000 m² of contributing area due to limitations in ALS topographic change detection under a forest canopy [Pelletier and Orem, 2014]. Erosion rates over the subannual time scale for each watershed were calculated by dividing the volume of change by the area of each upland watershed and the time interval over which the change took place. Data collected over approximately 1 year following the fire were combined to get an erosion rate directly relating to the post-wildfire erosion occurring in the watersheds.

Measurement uncertainty was estimated for each DEM and propagated through the differencing calculations. For all TLS-derived DEMs, the uncertainty of each elevation value was set to the maximum error associated with scan-to-scan registration performed in the Leica Cyclone software: 0.007 and 0.003 m and D1 and D2. For the prewildfire, vegetation point-derived DEM, the uncertainty was set to vary based on point cloud density between 0.007 m (the minimum uncertainty based on point cloud processing) and 0.03 m (the estimated maximum uncertainty based on nongeoreferenced error and estimated interpolation error). Therefore, cells within the DEM that had few points from which to derive a DEM elevation via interpolation were assigned a high uncertainty and those cells with many points were assigned a lower uncertainty.

The conditions for the TLS surveys were sufficiently ideal that the dominant errors were those associated with sensor accuracy. Passalacqua *et al.* [2015] identified several forms of additional uncertainty in multitemporal lidar studies, with the magnitude of uncertainty related primarily to the type and density of vegetation cover and the presence of steep slopes. The piedmont slopes we surveyed with TLS were modest (a few percent), and there were no large vegetation elements to cause occlusion (voids in the point cloud due to obstacles). As such, it is appropriate to consider the uncertainty to be dominated by the sensor accuracy.

3.2. Short-Term Erosion Rates From Non-Wildfire-Affected Watersheds Using Suspended Sediment Concentrations and Turbidity Data From Radiosondes

We estimated mean short-term (i.e., $\sim 10^0$ – 10^1 years) erosion rates using suspended sediment loads (SSLs) in five watersheds of similar area, relief, and lithology as D1 and D2 that have not experienced a wildfire since natural wildfire regimes occurred prior to 1900 [Dewar, 2011; Touchan *et al.*, 1996]: History Grove (HG), La Jara (LJ), Upper Jaramillo (UJ), Upper Redondo (UR), and Lower Redondo (LR) (Figure 1). SSL estimates were derived by developing a rating curve, i.e., a power law relationship between instantaneous sediment discharge and water discharge [Walling, 1974] (Figure 3) via repeated grab sample measurements of sediment concentrations approximately every 2 weeks from 2010 to 2012 and at a depth equal to 60% of the flow depth following Eads and Thomas [1983]. The rating curve was then used to estimate the sediment discharge time series over the 5 years of hydrograph data (Figure 3c). We performed the analysis using daily mean flows and hourly mean flows and obtained essentially identical results. The sediment discharge time series was then integrated and divided by the 5 year interval of study and the watershed area to obtain short-term erosion rates for non-wildfire-affected conditions in $\mu\text{m yr}^{-1}$ (Table 2). In addition, we estimated the geomorphic effectiveness [Wolman and Miller, 1960] of every flow in each of the five watersheds as the product of the frequency of each discharge event (obtained from a rank analysis) and the sediment discharge of that event.

Grab samples collected approximately every 2 weeks were collected over the full range of discharges recorded for each stream (Figure 3c). Grab samples were augmented with turbidity data for the History Grove watershed from radiosondes (described below), which provide a proxy for suspended sediment concentrations at 15 min intervals. As such, while individual storms were not intensively sampled manually, the turbidity data do provide some dense sampling.

Grab samples were collected in DI-washed 1000 mL High-density polyethylene (HDPE) bottles and sent to the University of Arizona (UA) for analysis. Samples were processed by centrifuging samples for 5 min at 3500 rpm to remove supernatant stream water from suspended sediment. The amount of water in each sample was measured using a 100 mL graduated cylinder. The remaining sediment was dried in an oven at 60°C, and the total mass of suspended sediment was measured.

A hydrogen peroxide treatment was used to remove organic material from SSL samples. SSL samples in 50 mL centrifuge tubes were placed in a warm-water bath under a fume hood. Three milliliters of 30% hydrogen peroxide (H_2O_2) was added to each sample, and the samples were gently swirled. Samples were allowed to react with hydrogen peroxide for approximately 12 h until another 3 mL of hydrogen peroxide was added. Hydrogen peroxide was added at 3 mL increments until no reaction (effervescence) was

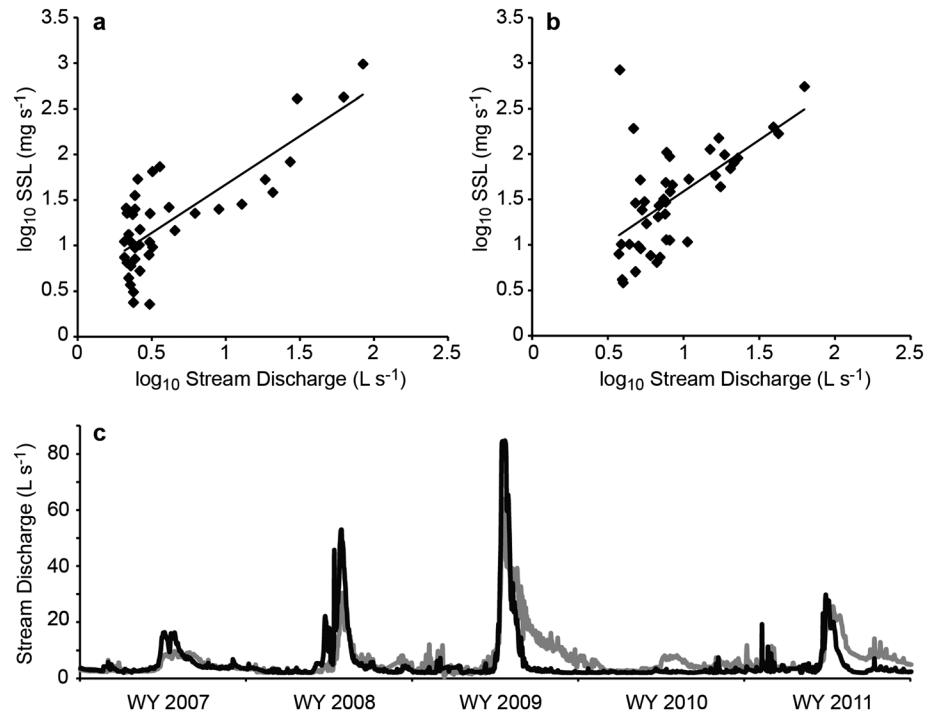


Figure 3. Graphs of the logarithm of measured suspended sediment load versus the logarithm of stream discharge values for the (a) History Grove and (b) La Jara watersheds. Rating curves (power law relationships) are shown by black lines. (c) Graph of stream discharge for History Grove (black line) and La Jara (gray line) watersheds used to calculate suspended sediment load.

Table 2. Rating Curve Coefficients (*a* and *b*) Based On a Power Law Relationship ($y = ax^b$) Between Suspended Sediment Load and Water Discharge, Sediment Yields, and Erosion Rates for the Five Non-Wildfire-Affected Watersheds for Each of the 5 Years of Measurement^a

Watershed	<i>a</i>	<i>b</i>	Year	Sediment Yield ($g\ m^{-2}\ yr^{-1}$)	Erosion Rate ($\mu m\ yr^{-1}$)
History Grove	4.040	1.064	2008	0.417 ± 0.099	0.278 ± 0.066
			2009	0.572 ± 0.101	0.381 ± 0.067
			2010	0.752 ± 0.101	0.501 ± 0.067
			2011	0.179 ± 0.099	0.119 ± 0.066
			2012	0.405 ± 0.099	0.270 ± 0.066
La Jara	2.860	1.133	2008	0.167 ± 0.089	0.111 ± 0.059
			2009	0.206 ± 0.089	0.137 ± 0.059
			2010	0.512 ± 0.089	0.341 ± 0.059
			2011	0.168 ± 0.087	0.112 ± 0.058
			2012	0.312 ± 0.086	0.208 ± 0.057
Upper Redondo	13.813	0.756	2008	1.797 ± 0.222	1.198 ± 0.148
			2009	1.515 ± 0.224	1.010 ± 0.149
			2010	1.406 ± 0.225	0.937 ± 0.150
			2011	4.038 ± 0.221	2.692 ± 0.147
			2012	1.269 ± 0.231	0.846 ± 0.154
Lower Redondo	5.032	1.027	2008	0.296 ± 0.024	0.197 ± 0.016
			2009	0.192 ± 0.024	0.128 ± 0.016
			2010	0.240 ± 0.024	0.160 ± 0.016
			2011	0.284 ± 0.023	0.189 ± 0.015
			2012	0.251 ± 0.023	0.167 ± 0.015
Upper Jaramillo	8.318	0.703	2008	0.428 ± 0.071	0.285 ± 0.047
			2009	0.432 ± 0.071	0.288 ± 0.047
			2010	0.528 ± 0.072	0.352 ± 0.048
			2011	0.303 ± 0.071	0.202 ± 0.047
			2012	0.458 ± 0.071	0.305 ± 0.047

^a ± values are uncertainties derived from equation (1).

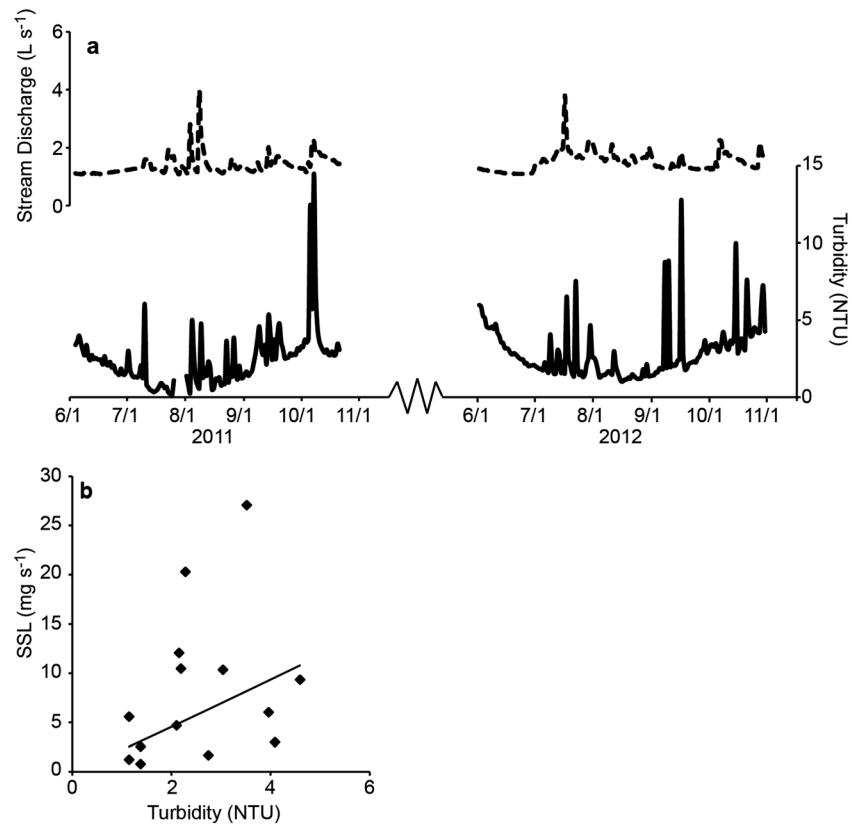


Figure 4. (a) Graph of stream discharge (dashed lines) and turbidity (solid lines) for the History Grove watershed over the 2011 and 2012 summer and monsoon seasons. (b) Graph of the measured suspended sediment load versus the turbidity values for the History Grove watershed used to establish a relationship between turbidity and SSL.

observed. The remaining sediment was dried in an oven at 60°C, and the total mass of nonorganic suspended material was measured.

The quasi-maximum likelihood estimator was used as a bias correction factor to correct for the general underestimation of SSL by the rating curve method [Ferguson, 1986]. An average soil density of 1.5 g cm⁻³ was used to convert the mass of sediment to volume [Kirchner et al., 2001; Meyer et al., 2001].

The uncertainties of the SSL-derived erosion rates were estimated by calculating the prediction intervals, i.e., confidence intervals for predicted values and future predicted values of a given regression, for the predicted erosion rates that were determined by applying the power law model to daily discharge data. Prediction intervals (e_p) for the predicted erosion rates were calculated at a 95% confidence interval using

$$e_p = t \cdot \hat{\sigma} \cdot \left(1 + \frac{1}{n} + \frac{(X_o - \bar{X})^2}{(n-1) \cdot s^2} \right)^{1/2} \quad (1)$$

where t is the t value assigned for the given degrees of freedom of the variable and a 95% confidence interval, $\hat{\sigma}$ is the mean root sum of squares, n is the number of samples, X_o is the sample discharge values, \bar{X} is the mean value of the sample discharge values, and s^2 is the variance [Ott and Longnecker, 2001]. The data were log transformed in order to apply a linear model instead of a power law model for the application of the prediction interval method. The resulting prediction intervals were back transformed (from linear to power law) and used to calculate uncertainties.

Turbidity data measured using radiosondes from the HG watershed (Figure 4) were used to estimate the short-term denudation rate in non-wildfire-affected areas for comparison to our SSL-derived erosion rates obtained using laboratory measurements of suspended sediment concentrations. Turbidity data were sampled at the HG watershed flume every 15 min during June through October when snow was not covering

Table 3. Location and Area Information for All Hydrologic Benchmark Network Watersheds Used in This Study

Watershed	Area (km ²)	Latitude ^a (°N)	Longitude ^a (°W)	Sediment Yield ^b (g m ⁻² yr ⁻¹)	Erosion Rate ^b (μm yr ⁻¹)
Merced River, CA	468.8	37.7317	119.5578	1.9 ± 1.2	1.3 ± 0.80
Mogollon Creek, NM	69.0	33.1667	108.6492	0.9 ± 0.8	0.62 ± 0.54
Wet Bottom Creek, AZ	36.4	34.1608	111.6922	1.2 ± 1.2	0.78 ± 0.80
Hayden Creek, ID	22.0	47.8228	116.6528	1.2 ± 0.6	0.80 ± 0.38
Sagehen Creek, CA	10.5	39.4317	120.2369	1.7 ± 1.4	1.1 ± 0.9
Rio Mora, NM	53.2	35.7772	105.6575	1.9 ± 1.1	1.2 ± 0.7
Halfmoon Creek, CO	23.6	39.1722	106.3886	3.6 ± 1.3	2.4 ± 0.9
South Twin River, NV	20.0	38.8875	117.2444	3.7 ± 6.4	2.4 ± 4.2
Encampment River, WY	72.7	41.0236	106.8242	3.9 ± 1.7	2.6 ± 1.1
Steptoe Creek, NV	11.2	39.2014	114.6875	8.4 ± 8.0	5.6 ± 5.3
Elder Creek, CA	6.5	39.7297	123.6428	11 ± 7.4	7.5 ± 4.9
Cache Creek, WY	10.6	43.4522	110.7033	16 ± 10	11 ± 6.9
Rock Creek, MT	850.0	48.9694	106.8389	4.2 ± 3.7	2.8 ± 2.5
Minam River, OR	621.6	45.6201	117.7256	6.7 ± 2.8	4.4 ± 1.8

^aLatitude and longitude given for outlet of watershed.

^bAverage value of all years on record, errors given as 1 standard deviation.

the landscape (Figure 4). Turbidity data have the advantage of a more complete sampling of the suspended sediment load than is possible using grab samples alone. One drawback of turbidity-based estimates of suspended sediment concentration is that organic and inorganic material cannot be distinguished. The same daily discharge data used in the SSL-derived denudation rate calculations were used to make a rating curve between stream discharge and turbidity data (measured in nephelometric turbidity units or NTUs). The rating curve was based on 267 daily average discharge and NTU samples. These samples were acquired from the 2011 and 2012 water years so that the same water years used to calculate the SSL-derived erosion rates were used to derive the erosion rates from the turbidity data. In order to estimate the SSL values, power law regression relationships between NTU values and SSL values were developed. From these regressions, the SSL values could be estimated from the NTU proxy values taken at the same time. The rating curve between discharge and turbidity data and the regression between turbidity proxy and SSL data were applied to stream discharge data for the 2008 to 2012 water years to estimate the sediment yield and erosion rates from the HG watershed.

Additional SSL data from 14 watersheds within the U.S. Intermountain West were also analyzed for comparison (Table 3) with the non-wildfire-affected erosion rates we estimated in the Valles Caldera. These watersheds are part of the U.S. Geological Survey (USGS) Hydrologic Benchmark Network (HBN) that has included 58 watersheds nationwide since its inception in 1963 [Clark *et al.*, 2000]. We selected 14 watersheds for rating curve analysis based on their small contributing areas (relative to other HBN stations; ranging from 6.5 km² to 850 km² (Table 3) but with most in the range of 6.5–100 km²), their location in the U.S. Intermountain West, and the availability of at least 25 years of data (most stations cover the period 1968–1996). Discharge and SSL data were obtained from the USGS National Stream Water-Quality Monitoring Network CD (1996). As with the SSL data from the Valles Caldera, we estimated the geomorphic effectiveness of every flow in each of the watershed as the product of the frequency of each discharge event (obtained from a rank analysis) and the sediment discharge of that event. This analysis demonstrates (see section 4.1) that the 25 years of record capture the geomorphically most effective floods for all 14 watersheds.

3.3. The Impact of Chemical Weathering on Short-Term Erosion Rates

Erosion occurs due to chemical and physical processes. Chemical processes typically dissolve rock and soil into its chemical components that are then transported from the watershed as solute load in runoff, while physical processes break down rock and soil into smaller pieces until the surface pieces can be entrained and transported from the watershed. In this study we compare physical erosion rates across time scales; hence, we must remove the chemical component from calculated erosion rates that include both the chemical and physical components. To remove the chemical component, we assume that short-term chemical erosion rates are representative of the long-term chemical denudation rates and use them to remove the chemical portion of the long-term denudation rate.

Table 4. Calculated Silica Solute Fluxes and Chemical Erosion Rates From Three Watersheds for the 3 Years When Solute Fluxes Were Measured

Watershed	Year	SiO ₂ Solute Flux ^a (g m ⁻² yr ⁻¹)	Erosion Rate ^a (μm yr ⁻¹)
History Grove	2010	1.225 ± 0.047	0.526 ± 0.020
	2011	0.273 ± 0.000	0.117 ± 0.000
	2012	0.722 ± 0.005	0.310 ± 0.002
La Jara	2010	1.071 ± 0.000	0.460 ± 0.000
	2011	0.331 ± 0.003	0.142 ± 0.001
	2012	0.749 ± 0.004	0.321 ± 0.002
Upper Jaramillo	2010	1.932 ± 0.099	0.830 ± 0.042
	2011	0.582 ± 0.015	0.250 ± 0.007
	2012	1.457 ± 0.009	0.625 ± 0.004

^aErrors given are 1 standard deviation.

Dissolved silica fluxes were used to calculate short-term (~10⁰ years), non-wildfire-affected erosion rates (corresponding to chemical processes only) for three watersheds on Redondo Mountain. Three watersheds with the requisite silica flux data were included in this analysis: History Grove, La Jara, and Upper Jaramillo (Figure 1). Stream water samples were collected during the 2010–2012 water years at weekly to monthly sample intervals during approximately March to October (no-snow conditions) by the UA Jemez River Basin Critical Zone Observatory. Samples were collected in acid-washed 1000 mL amber glass bottles and sent to the UA where they were stored at 4°C until analysis. Samples were filtered using HDPE-cased 0.45 μm nylon filters and transferred to 30 mL acid-washed HDPE bottles. All solute measurements were completed at the Arizona Laboratory for Emerging Contaminants at the UA.

Silica fluxes were calculated using a rating curve approach. A relationship between silica solute and daily discharge collected at stream gages was found in order to calculate a yearly silica flux in g m⁻² yr⁻¹ (Table 4). Daily discharge was collected at each sampling location using a pressure transducer at a flume with established rating curves. A silica density of 2.329 g cm⁻³ was used to convert the mass flux to a volume flux. The resulting silica flux-derived erosion rates for each of the 3 years and three watersheds are presented in μm yr⁻¹. An uncertainty for the resulting erosion rate is estimated by propagating an error of 5% of the SiO₂ value and 5% of the stream discharge value through the erosion rate calculations.

3.4. Long-Term Denudation Rates Derived From Cosmogenic ¹⁰Be in Channel Sediments

Mean denudation rates for a watershed can be calculated using ¹⁰Be where the bedrock is rich in quartz. The process involves measuring the concentration of ¹⁰Be in an amalgamated sample of sediment taken from different locations in the streambed at the outlet of a watershed. All samples from our watersheds were amalgamated samples that included five locations across an approximately 20 m length of streambed. By sampling a mixture of channel bed sediments, it is assumed that the sediment sample (i.e., quartz grains) is a relatively even mixture of from all portions of the upstream watershed. This is an appropriate assumption in watersheds, such as those in our study area, where landslides are not the dominant component of hillslope sediment transport.

Stream bed samples are then processed in the lab and the concentration of ¹⁰Be in the quartz measured. To calculate the denudation rate of the watershed, the production rate must also be calculated using known relationships between production rates and location characteristics (e.g., latitude, longitude, aspect, and elevation). Once both the concentration and the production rate are known (as well as other constants), the denudation rate can be calculated. We used this method in four watersheds within the study area to estimate denudation rates over a time scale of ~10³–10⁴ years (with lower time scales corresponding to higher measured erosion rates).

The watersheds included in this analysis are History Grove, La Jara, Upper Redondo, and Lower Redondo (Figure 1). Approximately two gallon-sized plastic bags of stream sediment were collected from the outlet flume location of each watershed. Sediment samples were brought to the UA where they were sieved to 0.25–0.5 mm. Samples were processed to accelerator mass spectrometry (AMS) targets at the UA following the instructions of the UC Santa Barbara Cosmogenic Nuclide Preparation Facility Sample Preparation

Table 5. Calculated ^{10}Be Concentrations and Denudation Rates for Four Watersheds

Watershed	Latitude Longitude (NAD 83)	Elevation (m)	Shielding Factor	Quartz Mass (g)	Be Carrier (mg)	$^{10}\text{Be}/^9\text{Be}$ Ratio ^a (10^{-13})	Production Rate ^b (Atoms yr^{-1})	^{10}Be Concentration ^c (10^3 Atoms g of Si^{-1})	Denudation Rate ^d ($\mu\text{m} \cdot \text{yr}^{-1}$)
History Grove ^e	35.8759 106.5125	2949	0.9941	9.3012	0.5471	2.23 ± 0.06	38.5 ± 1.9	438 ± 11.8	52.1 ± 3.0
La Jara ^e	35.8703 106.5273	3103	0.9893	9.9245	0.5033	2.48 ± 0.08	42.0 ± 2.1	420 ± 13.6	59.4 ± 3.6
Upper Redondo ^f	35.8929 106.5766	2999	0.9818	10.0492	0.5161	0.65 ± 0.04	39.5 ± 2.0	112 ± 6.9	212 ± 16.8
Lower Redondo ^f	35.8663 106.5978	2912	0.9786	10.0109	0.5245	0.71 ± 0.05	37.2 ± 1.9	124 ± 8.8	179 ± 15.5

^aMeasured at PRIME lab using a Beryllium standard 1000 $\mu\text{g}/\text{mL}$.

^bError approximated as 5%.

^cError includes propagated production rate error and concentration error.

^dNot corrected for inclusion of chemical denudation.

^eBlank for samples had a $^{10}\text{Be}/^9\text{Be}$ ratio of $1.87 \pm 0.17 \cdot 10^{-14}$.

^fBlank for samples had a $^{10}\text{Be}/^9\text{Be}$ ratio of $1.42 \pm 0.11 \cdot 10^{-14}$.

Manual and the guidance of the UA AMS Laboratory. AMS measurements were completed at the Purdue University PRIME Laboratory.

To calculate watershed-averaged denudation rates, the concentration of ^{10}Be in the sample and the production rate of ^{10}Be for the site were obtained. AMS-measured $^{10}\text{Be}/^9\text{Be}$ ratios were converted to ^{10}Be concentrations (atoms g^{-1}) (Table 5). The average production rate for each watershed was calculated by taking the average of calculated production rates for each pixel in a 10 m DEM. In this study we assume a constant production rate but correct for elevation, latitude [Lal, 1991], air pressure [Stone, 2000], and topographic shielding [Li, 2013] using separate corrections.

The ^{10}Be -derived denudation rates were corrected for the inclusion of chemical denudation by subtracting the chemical erosion rate calculated for the watershed or nearest watershed (section 3.3). Chemical erosion rates calculated for the HG and LJ watersheds were used to correct the ^{10}Be -derived denudation rates for those watersheds. However, chemical erosion rates calculated for the UJ watershed were used for the UR and LR watersheds because UJ was the closest watershed.

The time over which the ^{10}Be -derived denudation rates are averaged can be calculated by dividing the ^{10}Be cosmic ray absorption depth scale by the denudation rate. This approach assumes that most of the time involved in moving the sediment to the outlet of the watershed is spent eroding the sediment within the soil column and that surface transport from the soil column location to the watershed outlet is only a minor amount of time [von Blanckenburg, 2005]. An absorption depth scale of 0.6 m for cosmic rays was used in this study, based on an attenuation length of 160 g cm^{-2} and a density of 2.4 g cm^{-3} (density of rhyolite) [Gosse and Phillips, 2001]. Dividing the absorption depth scale for cosmic rays ($\approx 0.6 \text{ m}$) by the calculated erosion rates for each watershed gives the time scales over which the erosion rate is integrated [von Blanckenburg, 2005; DiBiase et al., 2010]. In this study the time scales range from approximately 3.1 and 3.7 kyr in the Upper Redondo and Lower Redondo watersheds, respectively, to approximately 11.3 and 12.8 kyr in the La Jara and History Grove watersheds, respectively.

The ^{10}Be -derived denudation rates calculated in this study represent erosion over Holocene time scales. Paleoenvironmental proxy data constrain the occurrence of periglacial activity in the region, e.g., colluvial deposits potentially indicative of periglacial processes on Redondo Mountain [Blagbrough, 1994], to be approximately 11,700 cal years B.P. in northern New Mexico [Armour et al., 2002]. Pollen records from the Jemez Mountains suggest that modern forest types had been established in the study area by approximately 10,500 cal years B.P. [Anderson et al., 2008]. The transition out of glacial climates and the establishment of the modern forest types by approximately the beginning of the ^{10}Be integration time interval indicate that erosion rates derived from this analysis are representative of Holocene erosional conditions.

3.5. Long-Term Denudation Rates Derived From Incision Into a Dated Paleosurface

Long-term ($\sim 10^6$ years) denudation rates were calculated by subtracting 10 m pixel^{-1} DEMs of modern topography from DEMs of paleosurfaces estimated by interpolating between modern topographic divides to calculate the “missing” or eroded volume from individual watersheds. These paleosurfaces are an estimate of the initial surface of Redondo Mountain prior to valley formation. In this section we provide an estimate

Table 6. Calculated High, Low, and Mean Denudation Rates for Four Watersheds Over the Total Landscape Age Using Incision Into a Dated Paleosurface

Watershed	Low Denudation Rate ($\mu\text{m yr}^{-1}$)	High Denudation Rate ($\mu\text{m yr}^{-1}$)	Denudation Rate ^a ($\mu\text{m yr}^{-1}$)
History Grove	16	24	19 ± 4
La Jara	29	37	32 ± 4
Upper Redondo	9	17	13 ± 4
Upper Jaramillo	17	25	20 ± 4

^aError is difference between average and high/low denudation rates.

of the erosion rate over million year time scales as a means of providing context to the Holocene erosion rates determined in section 3.4.

Denudation rates were calculated by dividing the estimated eroded volume by the area of the watershed and by the time interval, i.e., 1.24 Myr, the age of the landscape that coincides with the uplift of Redondo Mountain. This approach yields an order-of-magnitude estimate of denudation rate over the lifetime of the landscape since uplift began. History Grove, La Jara, Upper Redondo, and Upper Jaramillo were included in this analysis. Lower Redondo was not included because most of the watershed was formed by the structural development of a graben during resurgence of Redondo Mountain and not by fluvial or colluvial processes.

The subtraction of topographic surfaces and the integration of the missing volume were performed using the MATLAB software package. The pixels around the edge of each watershed were identified as tie points or boundary conditions, and a surface was interpolated among them using the TriScatteredInterp function within MATLAB. This function performs a Delaunay triangulation between a set of points identified by the user. The interpolated surface served as an estimate for the original surface of Redondo Mountain prior to valley formation. The denudation rate for each watershed was calculated by dividing the eroded volume by the area of the watersheds and by the time over which the denudation occurred. Because the resurgence of Redondo Mountain occurred within 27 kyr of the formation and eruption of the Valles Caldera at 1.25 Myr [Phillips *et al.*, 2007], an age of 1.24 Myr was used as the total denudation time for valley formation.

It is difficult to put a precise error estimate on this type of analysis. We added 10 m to the elevation of the topographic divides to represent the fact that the divides may have undergone up to ~10 m of erosion. This is reasonable considering that millennial-scale erosion rates are ~50 m Myr⁻¹, including both ridgetops and valley bottoms that have incised by as much as 100 m (erosion must have been higher in valley bottoms in order to form the valleys from an unincised initial condition). The high and low volumes (i.e., the volumes calculated with and without 10 m added to the paleosurface reconstruction) were used to calculate denudation rates and then averaged to get a single denudation rate for each watershed (Table 6). The error prescribed to the denudation rates was approximated by the difference between the average denudation rate and the denudation rate derived from the high and low volumes. As with the long-term, ¹⁰Be-derived denudation rates, the calculated paleosurface incision-derived rates were corrected for the inclusion of chemical denudation rates by subtracting the calculated chemical erosion rates for each watershed.

3.6. Model Calculations

Given measured erosion rates from wildfire-affected and non-wildfire-affected watersheds, as well as measured denudation rates over geologic time scales, it is possible to estimate the recurrence interval (RI) of high-severity wildfires most consistent with the measured differences among short-term erosion rates and long-term denudation rates. These estimates can then be compared to independent data for RI values from proxies for high-severity wildfires to check for consistency.

We assume in our analysis that post-wildfire erosion is dominated by high-severity wildfires. This is a reasonable assumption given the strongly nonlinear relationship between erosion and burn severity [Pelletier and Orem, 2014]. Also, this is a conservative approach because adding the erosional effects of low- and moderate-severity wildfires would only increase the relative importance of wildfire-affected erosion over and above our analysis, which considers the effects of high-severity wildfires only. Similarly, we assume that short-term erosion rates are dominated by the frequent events captured by the 5 years of SSL data. In section 4.2 we show that the geomorphically most effective events occur at a sufficiently large fraction of

Table 7. Mean Erosion and Denudation Rates and Associated Time Intervals of Measurement^a

Site	Time Interval (Year)	SSL ^b Erosion Rate ($\mu\text{m yr}^{-1}$)	Time Interval (Year)	TLS and ALS ^c ($\mu\text{m yr}^{-1}$)	Time Interval (kyr)	¹⁰ Be-Derived ^d Denudation Rate ($\mu\text{m yr}^{-1}$)	Time Interval (Myr)	Topo ^e ($\mu\text{m yr}^{-1}$)
HG	5	0.310 ± 0.067			12.8	52.1 ± 3.0	1.24	19 ± 4
LJ	5	0.182 ± 0.058			11.3	59.4 ± 3.6	1.24	32 ± 4
UR	5	1.337 ± 0.150			3.1	212 ± 16.8	1.24	13 ± 4
LR	5	0.168 ± 0.016			3.7	179 ± 15.5		
UJ	5	0.286 ± 0.047					1.24	20 ± 4
D1			1	12,000 ± 4,100 ^f 23,000 ± 1,000 ^g				
D2			1	660 ± 160 ^f 12,000 ± 500 ^g				

^aAll rate uncertainties are estimates of the measurement uncertainty.

^bSuspended sediment load (SSL).

^cLight detection and ranging (lidar).

^dCosmogenic radionuclide (CRN).

^eFrom incision into a dated paelosurface.

^fEstimate derived from TLS data.

^gEstimate derived from ALS data.

the time that they are common events in our data set. Moreover, events larger and rarer than the effective discharge systematically decrease in effectiveness for the range of discharges captured in our data set. Moreover, we show in section 4.4 that our results regarding the relative importance of wildfire-affected erosion on the long-term denudation of the landscape are robust with respect to even order-of-magnitude uncertainties in the relative erosion rates between wildfire-affected and non-wildfire-affected conditions.

We computed the fraction of time associated with wildfire-affected conditions (f_{WA}) using a weighted mean relationship:

$$D = E_{NWA} \cdot (1 - f_{WA}) + E_{WA} \cdot f_{WA} \tag{2}$$

where D is the long-term denudation rate and E_{WA} and E_{NWA} are the wildfire-affected and non-wildfire-affected erosion rates, respectively (Table 7). The value of D was set equal to long-term denudation rates derived from ¹⁰Be analysis. Then, the recurrence interval RI was calculated from the definition of f_{WA} , i.e.,

$$f_{WA} = \frac{t_R}{RI} \tag{3}$$

where t_R is the time scale of recovery over which erosion rates return to non-wildfire-affected levels following a wildfire using an exponential decay model (described in more detail in section 4.2). The relative importance of wildfire-affected denudation, P_{WA} , was then computed as the fraction of time that wildfire conditions were active multiplied by the ratio of the wildfire-affected erosion rate to the long-term denudation rate, i.e.,

$$P_{WA} = f_{WA} \frac{E_{WA}}{D} \tag{4}$$

4. Results

4.1. Short-Term Erosion and Long-Term Denudation Rates

Short-term ($\sim 10^0$ – 10^1 years) erosion rates in recently non-wildfire-affected watersheds vary from $0.182 \pm 0.058 \mu\text{m yr}^{-1}$ to $1.337 \pm 0.15 \mu\text{m yr}^{-1}$ (Figure 5 and Tables 7). Erosion rates estimated during the summer months using turbidity data with fine temporal resolution (15 min) yield even lower rates (Table 8), consistent with the hypothesis that most of the erosion during the year is associated with periods of snowmelt. The range of erosion rates computed from SSL data is slightly lower than but broadly consistent with rates calculated from the USGS HBN stations using daily mean flows, which range from $0.62 \pm 0.54 \mu\text{m yr}^{-1}$ to $11 \pm 6.9 \mu\text{m yr}^{-1}$ (Table 3). Although USGS HBN stations represent a wide range of tectonic, geologic, and climatic environments and they are much larger in area than the watersheds we studied, data from these stations are useful to present here because they demonstrate that the erosion rates from the Valles Caldera are approximately of the same order as the values obtained from other locations in the U.S. Intermountain West obtained using similar data.

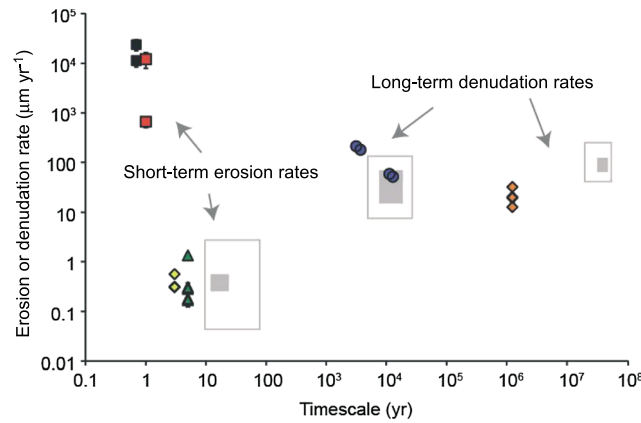


Figure 5. Plot of the erosion or denudation rate for each watershed calculated using the different methods applied in this study versus the time scale of measurement. Short-term wildfire-affected, TLS- and ALS-derived erosion rates (red and black squares, respectively), non-wildfire-affected, SSL-derived erosion rates (green triangles), chemical flux-derived erosion rates (yellow diamonds), and long-term ¹⁰Be-derived denudation rates (blue circles) and denudation rates derived from incision into a paleosurface (orange diamonds) are shown. Data from Kirchner *et al.* [2001] are also shown in gray for comparison with the outer rectangle showing the full range in the data and the inner filled rectangle showing the middle 50% of the data.

Short-term erosion rates in recently wildfire-affected watersheds vary from $660 \pm 160 \mu\text{m yr}^{-1}$ to $23,000 \pm 1000 \mu\text{m yr}^{-1}$ (Figure 5 and Table 7). In the year following the wildfire, erosion rates increased by more than 3 orders of magnitude above those associated with non-wildfire-affected conditions.

Figure 6a plots the relative geomorphic work as a function of the flow duration, i.e., the fraction of time that flows equal to or greater than a given discharge occurs. The effective discharge is defined by the peak in these graphs. Figure 6a demonstrates that the effective discharge in our study site has a flow duration of between approximately 50% and 90%. These results are consistent with the hypothesis that base flows and snow-melt periods are responsible for the vast majority of the sediment exported from our study watersheds in the absence of wildfire.

The results in Figure 6a differ from most studies of effective discharge, which generally conclude that flows equal to or greater than the effective discharge occur between 0.1 and 10% of the time [Wolman and Miller, 1960; Andrews, 1980; Andrews and Nankervis, 1995]. However, our results are consistent with at least one study from a landscape with porous soils and predominantly groundwater flow. Ma *et al.* [2010] calculated flow durations of between 18 and 92% for the effective discharges of watersheds incised into eolian sand deposits of the Wuding River basin, China. Ma *et al.* [2010] proposed that the highly porous nature of the deposits contributed to an unusually large ratio of subsurface to surface flow and hence a relatively low discharge variability. Our study site differs in many ways from that of Ma *et al.* [2010], but the highly fractured nature of the Valles Caldera tuff and rhyolite leads to a similarly dominant groundwater flow regime with relatively low discharge variability [Zapata-Rios *et al.*, 2015].

Figure 6b shows the analogous results for the USGS HBN stations, again demonstrating that the effective discharge occurs at sufficiently large fraction of time (ranging from approximately 0.01 to 0.15) that many such discharges are included in the 25 years of data available. Moreover, Figures 6a and 6b demonstrate a systematic decrease in geomorphic effectiveness with decreasing flow duration for all of the watersheds we studied.

Long-term denudation rates measured over time scales of $\sim 10^3$ – 10^4 years and $\sim 10^6$ years ranged from $13 \pm 4 \mu\text{m yr}^{-1}$ to $212 \pm 16 \mu\text{m yr}^{-1}$ (Figure 5 and Table 7). Denudation rates calculated by ¹⁰Be analysis are somewhat higher than denudation rates estimated using incision into a dated paleosurface over the last ~ 1.24 Myr. ¹⁰Be-derived denudation rates are of the same order of magnitude as those in similar studies

Table 8. Sediment Yields and Erosion Rates Calculated From Turbidity Data (NTU) for the History Grove Watershed for 5 Years

Watershed	Year	Sediment Yield ^a ($\text{g m}^{-2} \text{yr}^{-1}$)	Erosion Rate ^a ($\mu\text{m yr}^{-1}$)
History Grove	2008	0.066 ± 0.003	0.044 ± 0.002
	2009	0.065 ± 0.003	0.044 ± 0.002
	2010	0.065 ± 0.003	0.044 ± 0.002
	2011	0.062 ± 0.003	0.041 ± 0.002
	2012	0.065 ± 0.003	0.043 ± 0.002

^aErrors approximated as 5% of the value.

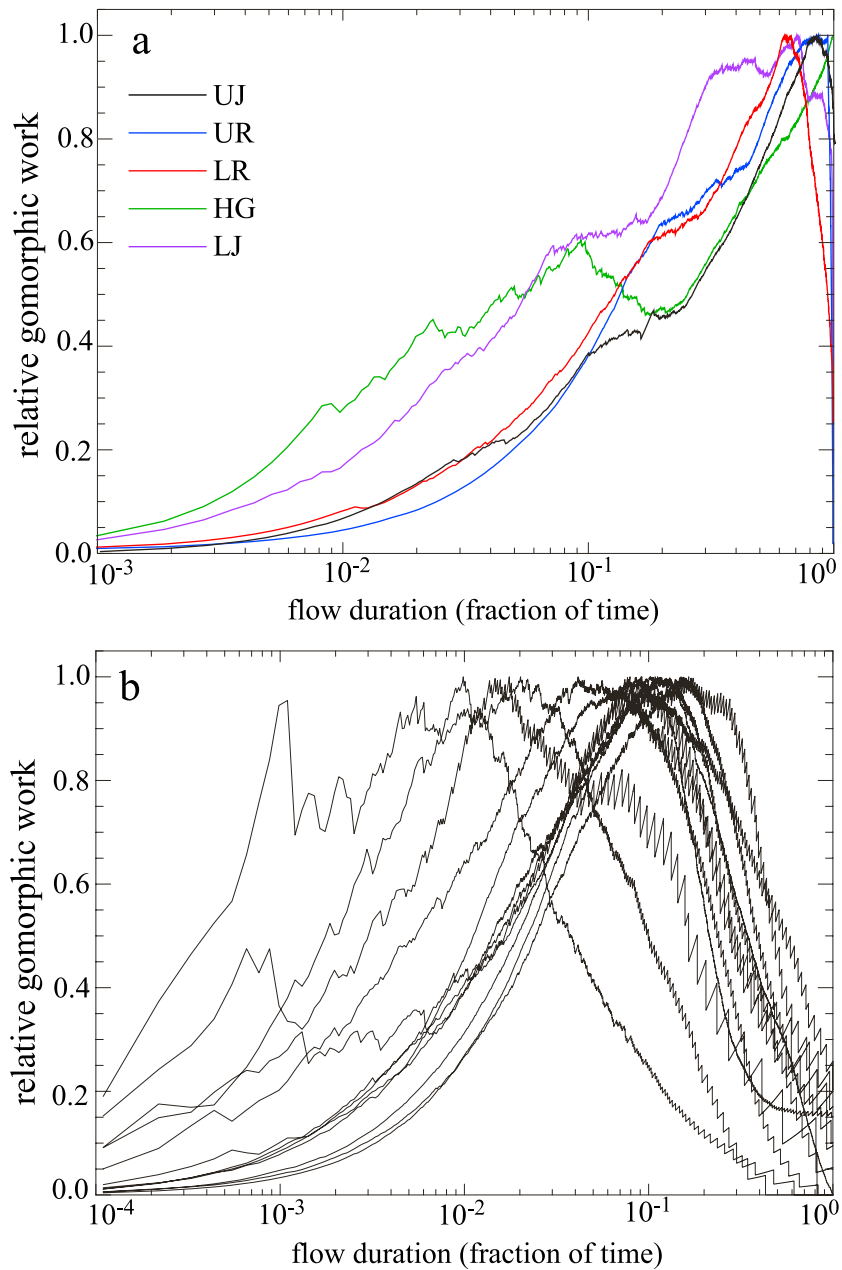


Figure 6. Plot of the relative geomorphic work of floods, i.e., the sediment transport estimated from the rating curve multiplied by the frequency of each event (normalized by the maximum value for each watershed) as a function of the flow duration (i.e., the fraction of time that flows greater than or equal to that discharge occur). (a) Valles Caldera data. (b) USGS HBN station data.

within the western U.S. [Granger *et al.*, 1996; Riebe *et al.*, 2000; DiBiase *et al.*, 2010] and represent an average rate over time scales ranging from 3.1 to 12.8 kyr.

4.2. Mean Post-wildfire Recovery Time Scale

Orem and Pelletier [2015] demonstrated that the export of sediment from watersheds D1 and D2 to their adjacent piedmont surfaces decreases exponentially with time with a time constant of approximately 1 year. The increase in erosion rate above background associated with a single high-severity wildfire is thus given by

$$(E_{WA} - E_{NWA}) \int_0^{\infty} e^{-t/t_R} dt = (E_{WA} - E_{NWA}) \cdot t_R. \tag{5}$$

Table 9. Averaged Erosion Rate Values and Calculated RI, f_{WA} , and P_{WA} Values

Site	D ($\mu\text{m yr}^{-1}$)	E_{NWA} ($\mu\text{m yr}^{-1}$)	E_{WA} ($\mu\text{m yr}^{-1}$)	Time Interval (kyr)	RI ^a (Year)	f_{WA} ^b	P_{WA} ^c
HG and LJ							
Using TLS E_{WA}	55 ± 3	0.246 ± 0.063	$6,400 \pm 2,200$	12.1	115	0.008	0.996
Using ALS E_{WA}			$17,000 \pm 8,700$		313	0.003	0.993
UR and LR							
Using TLS E_{WA}	195 ± 16	0.753 ± 0.083	$6,400 \pm 2,200$	3.4	33	0.031	0.996
Using ALS E_{WA}			$17,000 \pm 8,700$		90	0.011	0.991

^aCalculated using equation (3).
^bCalculated using equation (2).
^cCalculated using equation (4).

Equation (5) demonstrates that in the exponential decay model for post-wildfire erosion, elevated erosion rates persist for time periods longer than t_R , but the cumulative effect of post-wildfire denudation is equivalent to that of a constant erosion rate acting over a time interval t_R . One of the two watersheds we monitored with TLS did not show as systematic an exponential decrease in sediment yield (e.g., D2) with time following the wildfire as the other, a fact we attributed to the precise timing of storm events within the recovery period [Orem and Pelletier, 2015]. However, the data from both watersheds show a characteristic decrease in sediment flux with the time scale of approximately 1 year. The stochastic nature of rainfall therefore gives rise to significant variability in how precisely the data fit an exponential model and in resulting best fit values of t_R , variability that we address in the Monte Carlo analysis of section 4.4.

Our measured t_R value of approximately 1 year [Orem and Pelletier, 2015] is consistent with three recent analyses of recovery times following wildfires in the western U.S. Moody [2012] obtained a mean recovery time of approximately 0.8 year (his Figure 10). Similarly, Wagenbrenner and Robichaud [2014] quantified the decrease in erosion rate above background for two postfire years and showed large successive decreases in erosion rates from each year to the next following wildfires, with values near background level after 2 years. Finally, Santi and Morandi [2013] concluded based on their study of 900+ debris flows that “it takes approximately 1 year, or at a few locations, as much as 3 years, for debris production to return to prefire rates.”

4.3. Model Calculations

Computed values of the fraction of long-term denudation resulting from wildfire-affected conditions, P_{WA} , range from 0.991 to 0.996. Four different estimates are available corresponding to whether we use the average erosion rate value for the D1 and D2 watersheds measured by TLS ($6400 \pm 2200 \mu\text{m yr}^{-1}$) or ALS ($17000 \pm 8700 \mu\text{m yr}^{-1}$) and whether we use the relatively low average ^{10}Be -derived denudation rate for the south draining watersheds of HG and LJ ($55 \pm 3 \mu\text{m yr}^{-1}$), the relatively high average ^{10}Be -derived denudation rate for the north draining watersheds of UR and LR. For each scenario, equations (2)–(4) provide a value for the recurrence interval of high-severity wildfire required to close the denudation rate budget. Values of RI predicted by equations (2)–(4) range from 33 to 313 years (Figure 5 and Table 9). In section 5.4 we compare these predicted recurrence intervals to independent constraints from proxy data. All calculations were completed using a mean recovery time of 1 year and the average short-term non-wildfire-affected erosion rate of the watersheds involved in each calculation. In the Monte Carlo analysis of the next section we consider the impact of uncertainty in the parameter values on the values of P_{WA} .

4.4. Sensitivity of the Conclusions With Respect to Uncertainties

To determine the sensitivity of P_{WA} values with respect to uncertainties in the parameter values, we simulated multiple sets of 10,000 hypothetical long-term histories, each representing an interval of geologic time with a mixture of “background” non-wildfire-affected erosion and infrequent but intense postfire erosion. The output of each realization is the fraction of total denudation associated with wildfire-affected conditions for each realization with different mean values of t_r , E_{NWA} , E_{WA} , and D for a hypothetical history. This type of analysis is necessary because while we measured an increase of 10^3 – 10^5 in erosion rates following the Las Conchas fire, that fire might be unusual in terms of the magnitude of the response and/or the speed at which erosion rates returned to those associated with non-wildfire-affected conditions. As such, it is crucial to determine whether our conclusions regarding the relative importance of wildfire-affected erosion on the long-term denudation

of the landscape would hold if the mean increase in erosion rates following wildfires were only the range of 10^2 – 10^4 , for example, instead of 10^3 – 10^5 .

We performed the first set of 10,000 simulations using a default set mean values equal to 1 year, $1 \mu\text{m yr}^{-1}$, $10,000 \mu\text{m yr}^{-1}$, and $100 \mu\text{m yr}^{-1}$ for the recovery time scale (t_r), the short-term denudation rate associated with non-wildfire conditions (E_{NWA}), the short-term denudation rate associated with wildfire conditions (E_{WA}), and the long-term denudation rate (D), respectively. For each realization the parameter values were sampled from lognormal distributions with coefficients of variation equal to 1 for all of the variables except for E_{WA} , where we used a coefficient of variation equal to 3 to represent the larger variability in post-wildfire denudation rates relative to the other parameters. These coefficients of variation are not uniquely constrained, but this fact does not negate the value of the analysis, which is to show how sensitive the P_{WA} values are to variations and/or uncertainties in the model parameters. The output of the analysis is a frequency distribution of values for P_{WA} , the fraction of total physical denudation associated with wildfire-affected conditions (Figure 7e). This figure shows that in all cases, the most probable P_{WA} value exceeds 0.99 and the probability of obtaining a P_{WA} value lower than 0.9 is very small (approximately 1%).

Figures 7a–7e plot variations in t_r , E_{NWA} , E_{WA} , D , and the resulting value of P_{WA} for the first 100 simulations with the default set of parameters. Figure 7e plots the frequency distribution of the resulting P_{WA} value for all 10,000 simulation runs with the default set of parameters. We also ran two additional sets of 10,000 simulations corresponding to alternative mean values for E_{WA} ($1000 \mu\text{m yr}^{-1}$ instead of $10,000 \mu\text{m yr}^{-1}$), and then, in addition, we changed the mean value of t_r to 3 years instead of 1 year. The point of these alternative sets of simulations is to address the possibility that the Las Conchas wildfire is an extreme event in terms of the magnitude of the erosional response above non-wildfire-affected conditions and/or the time scale of recovery. The results for these alternative cases follow a similar distribution to that of the default case: all but approximately 1% of these 20,000 alternative cases have P_{WA} larger than 0.90 (Figure 7e).

5. Discussion

5.1. Incompleteness of the TLS Data and Its Potential Impact on Short-Term Erosion Rates in Wildfire-Affected Watersheds

The TLS-derived short-term wildfire-affected erosion rates are minimum values due to incomplete preservation of material on the piedmont surface (some material passed through the survey area) and incomplete survey coverage of the depositional area. Our TLS surveys each included 10–20 scan stations that cover the vast majority of the area of deposition, but the surveys did not include some thin (~ 1 cm) deposits near the edge of the depositional area. However, these areas were primarily organic material deposits (grass, pine needles, and small twigs) that are not relevant to estimating erosion rates. We infer that our minimum estimates for the volume of deposited sediment are close to the actual volume of sediment derived from the watersheds because our surveys cover nearly the entire area of significant clastic deposition and because the main incised channels created on the two piedmonts (the only channels that could have transported sediment past the piedmont) do not extend to the East Fork Jemez River (Figure 1). ALS-derived erosion rates could also be biased since they include only erosion and deposition that occurred within the first year following the wildfire and vertical changes < 0.3 m were filtered out of the analysis.

5.2. Representativeness of the SSL Data for Measuring Short-Term Erosion Rates in Non-Wildfire-Affected Watersheds

We did not measure bed load, thus introducing uncertainty into our estimate of E_{NWA} . Bed load is difficult to measure completely, as even slot samplers do not sample the entire range of bed material particle sizes [e.g., Nichols *et al.*, 2008] and detention basins may overflow during large events [e.g., Kirchner *et al.*, 2001]. To address this issue, we use the results of two published studies from small forested watersheds that suggest that the relative importance of bed load is likely to be small relative to the 3–5 orders of magnitude increase we measured between wildfire-affected and non-wildfire-affected conditions. Both studies constrain the ratio of bed load to suspended load in forested watersheds of similar area (i.e., 1–10 km²) that were subjected to disturbance. Grant and Wolff [1991] measured bed load to be between 8 and 38% of the total load in three watersheds in the H.J. Andrews Experimental Forest in Oregon. Ferguson and Stott [1987] found bed load to be less than 2% of the total load in two watersheds of similar area in Scotland. Based on these studies, we

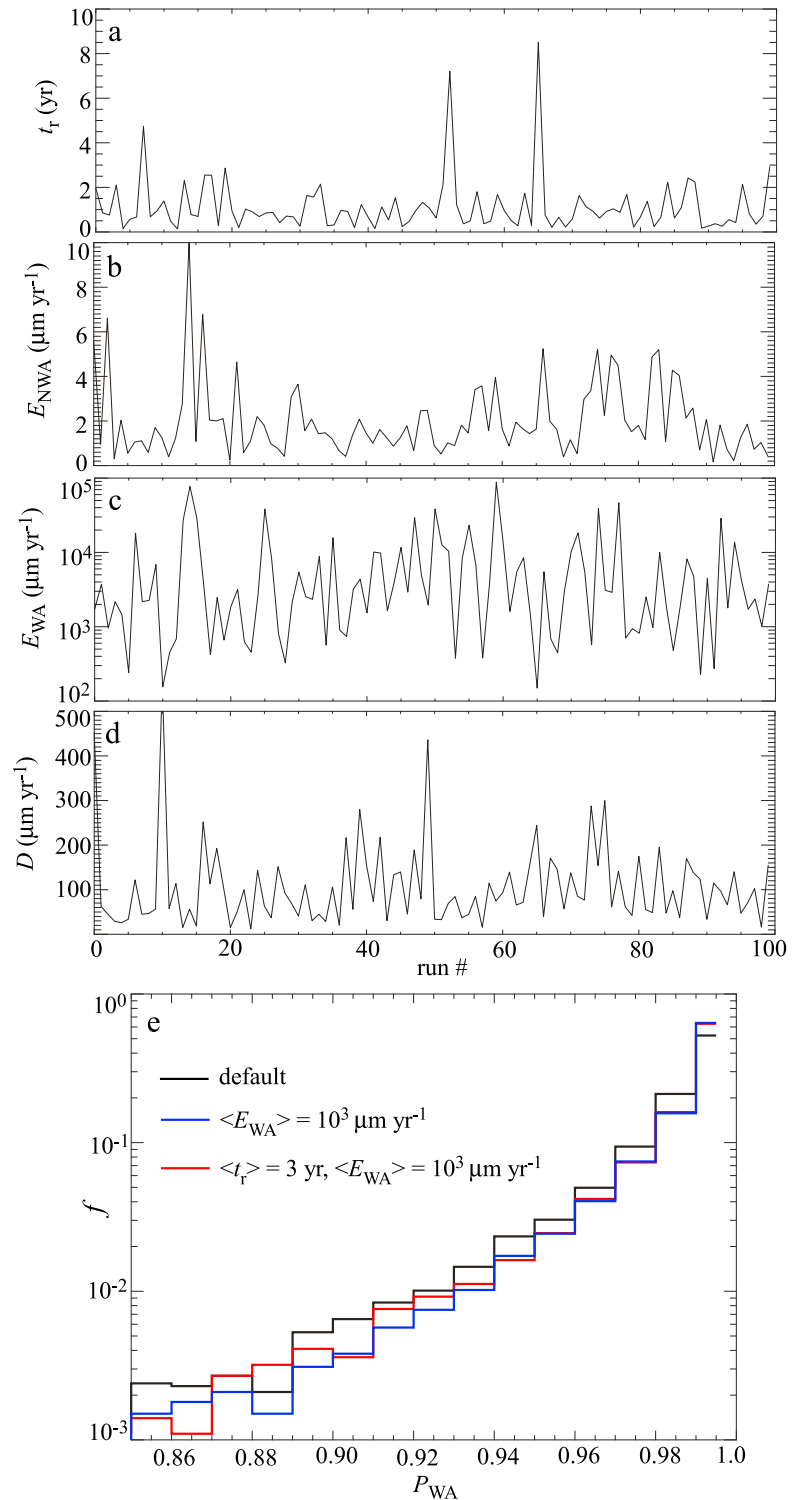


Figure 7. Results of the Monte Carlo simulations. (a–d) Plots of the parameter values in equations (2)–(4) sampled from lognormal distributions (with mean values of 1 year, $1 \mu\text{m yr}^{-1}$, $10,000 \mu\text{m yr}^{-1}$, and $100 \mu\text{m yr}^{-1}$, respectively, and coefficients of variation equal to 1 for all parameters except E_{WA} (a coefficient of variation of 3 was selected for this parameter to reflect its larger variability in nature)) for the first 100 simulation runs. (e) Histogram of the frequency of occurrence of P_{WA} from all of the 10,000 runs using mean values of t_r , E_{NWA} , E_{WA} , and D equal to 1 year, $1 \mu\text{m yr}^{-1}$, $10,000 \mu\text{m yr}^{-1}$, and $100 \mu\text{m yr}^{-1}$, respectively (default case). Also shown is the histogram resulting from lowering the mean E_{WA} value to $1000 \mu\text{m yr}^{-1}$ (keeping other mean values the same as the default case) and the histogram resulting from lowering the mean E_{WA} value to $1000 \mu\text{m yr}^{-1}$ and increasing the mean t_r value to 3 years.

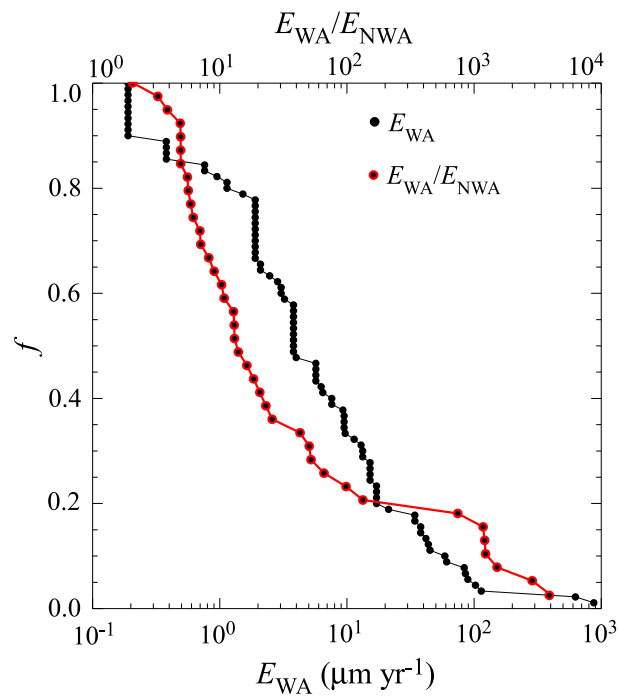


Figure 8. Cumulative frequency-magnitude plots of the number of studies (90 in total) that have reported short-term erosion rates from U.S. forests with minimal (<5% of area) human disturbance (some of which are wildfire affected) and E_{WA}/E_{NWA} values (with E_{WA} measured within the first year following the wildfire) greater than the values plotted on the x axis. Data are from the literature review of Fowler [1979].

[Blankenburt, 2005]. However, the rates we obtained are consistent with a century of work measuring short-term erosion rates in U.S. forest areas with minimal human disturbance. The most recent compilation of short-term erosion rates reported in the literature from U.S. forests is Montgomery [2007], who reported the following values (from his SI Table 6): $<10 \mu\text{m yr}^{-1}$ [Blakely et al., 1957], $0.21 \mu\text{m yr}^{-1}$, $1.9 \mu\text{m yr}^{-1}$, $680 \mu\text{m yr}^{-1}$ [Fowler and Heady, 1981], $0.41 \mu\text{m yr}^{-1}$ [Pimentel et al., 1976], and $2.1 \mu\text{m yr}^{-1}$ [Pimentel et al., 1976]. The only value substantially larger than the E_{NWA} values we report here is the $680 \mu\text{m yr}^{-1}$ value of Fowler and Heady [1981]. However, the three data points that Montgomery [2007] cites from Fowler and Heady [1981] are not measured sediment yields. Instead, they are the range of typical (0.21 – $1.9 \mu\text{m yr}^{-1}$) and the maximum ($680 \mu\text{m yr}^{-1}$) yields predicted from a statistical model of sediment yields in undisturbed U.S. forests (defined by Fowler and Heady [1981] as those with <5% area disturbed by direct human activities such as logging or construction; thus, they include wildfire and other natural disturbance processes) calibrated using a remarkable compilation of 90 measured sediment yields in undisturbed U.S. forests [Fowler, 1979].

Figure 8 presents the cumulative frequency distribution of the 90 short-term erosion rates of undisturbed U.S. forests reported by Fowler [1979]. As noted above, these studies include the effects of wildfire and other natural disturbance processes. Approximately 20% of these studies report short-term erosion rates of $<1 \mu\text{m yr}^{-1}$. Of the remaining studies with short-term erosion rates $>1 \mu\text{m yr}^{-1}$, Fowler [1979] demonstrated that nearly all of these areas were associated with the occurrence of wildfire and/or landsliding. Figure 8 also plots the ratio of wildfire-affected to non-wildfire-affected short-term erosion rates in the first year after the wildfire from the 39 studies Fowler [1979] compiled in which such data were available. Figure 8 shows that the E_{WA}/E_{NWA} values range from $\sim 10^0$ to 10^4 . Our measured values for the relative increase in wildfire-affected denudation, which range from $\sim 10^3$ to 10^5 , are at or just above the high end of this range. The fact that our data occur at the high end of Fowler's [1979] range is consistent with the fact that he included watersheds in which any portion was affected by wildfire. In contrast, watersheds D1 and D2 were burned at high severity over the majority of their contributing area, resulting in a geomorphic response at the high end of the spectrum.

conclude that bed load is likely to be, at most, half of the total load in our study site. As such, the error in neglecting bed load is far less than the 3–5 orders of magnitude increase due to wildfire.

5.3. Comparison of Short-Term Erosion Rates With Published Values From Similar Landscapes

E_{WA} values and their increase above E_{NWA} values are comparable to values reported from wildfire-affected areas in previous studies [Kirchner et al., 2001; Meyer et al., 2001; Istanbulluoglu et al., 2003; Malmon et al., 2007; Shakesby and Doerr, 2006; Wagenbrenner and Robichaud, 2014] (i.e., $\sim 10^2$ – $10^4 \mu\text{m yr}^{-1}$ and a 2–5 orders of magnitude increase from non-wildfire-affected to wildfire-affected erosion rates). E_{NWA} values reported for our study site are comparable to, or only slightly lower than, SSL-derived erosion rates calculated for other small, mountainous watersheds in the Intermountain West over similar time scales (Table 3).

The E_{NWA} values may seem unrealistically low. Indeed, these rates are comparable to the lowest rates measured anywhere on Earth over geologic time scales [von

5.4. Independent Constraints on Recurrence Intervals of High-Severity Wildfire

The recurrence intervals (RIs) of high-severity wildfires required to close the denudation rate budget, i.e., 33–313 years, are comparable to independent constraints from the Valles Caldera region specifically and from the U.S. Intermountain West, in general. Frequency distributions of even-aged stands provide constraints on the recurrence intervals of high-severity (i.e., stand replacing) wildfires. Charcoal-rich deposits in alluvial fans and other depositional zones can also constrain the recurrence intervals of moderate- and high-severity wildfires. The severity of the wildfire that triggered deposition can be broadly inferred from the thickness and texture of the deposits. For example, *Pierce and Meyer* [2008] state “We define ‘large fire-related events’ as events represented by debris flow units with abundant coarse angular charcoal that are generally coarser grained than other units in a stratigraphic section and comprise at least 20% of the thickness of the section [*Pierce et al.*, 2004]. These deposits are often underlain by burn surfaces and most likely represent high-severity burns.”

Allen et al. [2008] obtained a wildfire recurrence interval of 200 years in Chihuahueños bog and 111 years in Alamo bog in the Valles Caldera region over the past 15 kyr. *Allen et al.* [2008] did not constrain the severity of these wildfires, but given that they triggered charcoal-rich deposition in the center of a low-relief basin together with the fact that RI values from fire scar records (indicative of low- to moderate-severity wildfires) from the same area were much smaller, it is probable that these events represent high-severity wildfires.

High-severity wildfires from other conifer forests of the U.S. Intermountain West have recurrence intervals of approximately 150 to 400 years based on frequency distributions of even-aged stands and fire-related sedimentation studies [*Meyer et al.*, 1995; *Veblen, et al.*, 1994; *Kipfmüller and Baker*, 2000; *Sibold et al.*, 2006; *Margolis et al.*, 2007; 2011; *Fitch and Meyer*, 2015]. We conclude that RI values required to close the long-term denudation rate budget (which have a median value of 211 years) for the study area are broadly consistent with RI values measured independently. Note that these RI values for high-severity wildfires were not used to calculate the P_{WA} reported in Table 9 but are merely an independent check on the results.

5.5. Potential Application to Other Landscapes

Previous studies that have quantified the relative importance of wildfire-affected erosion in the long-term denudation of landscapes have generally attributed a lower percentage, i.e., between 30 to 77%, to wildfire-affected conditions [*Meyer et al.*, 1995; *Pierce et al.*, 2004; *Fitch and Meyer*, 2015; *Weppner et al.*, 2003; *Riley et al.*, 2015]. As noted in section 1, however, actual estimates could be higher or lower than these values. The results of this paper depend heavily on the assumption that debris flows do not export sediment from watersheds $> \sim 1 \text{ km}^2$ in area in the absence of wildfire. This assumption is defensible for this particular study area for the reasons stated in section 2, i.e., modest slopes for 90% of the landscape and a relative absence of bare ground. However, in areas where long-runout debris flows are common in the absence of wildfire, it is reasonable to expect that wildfire-affected erosion would not be the predominant driver of long-term denudation. The conclusions of this paper are consistent with the modeling results of *Istanbulluoglu et al.* [2004] of a study region in Idaho, where wildfire-affected conditions were estimated to be responsible for 92% of long-term denudation.

6. Conclusions

Our analysis, which combines data for erosion rates measured over short time scales in wildfire-affected and non-wildfire-affected watersheds with long-term denudation rates, demonstrates that post-wildfire erosion is responsible for the vast majority ($>90\%$) of denudation in the Valles Caldera over geologic time scales. The range of wildfire RI values required to close the denudation rate budget agrees well with published values for high-severity wildfires based on frequency distributions of even-aged tree stands and fire-related sedimentation records. Given that our analysis is robust with respect to large variations in the ratio of wildfire-affected to non-wildfire-affected erosion rates, together with the fact that wildfire-induced increases of up to 3 orders of magnitude are standard [*Wagenbrenner and Robichaud*, 2014], it is possible that wildfire-affected erosion may dominate in other conifer-forested upland watersheds $>1 \text{ km}^2$ in area in which sediment export from watersheds is not dominated by debris flows in the absence of wildfire.

Acknowledgments

All fieldwork was conducted through collaboration between the UA JRB-SCM Critical Zone Observatory funded by NSF EAR-0724958 and EAR-1331408 and the Valles Caldera National Preserve. A GSA Graduate Student Research Grant provided funding for ^{10}Be analyses. We thank Dick Heermance and Li Cheng for their guidance on the ^{10}Be methodology and Jennifer McIntosh for sharing silica solute flux data. We wish to thank Editor John Buffington, Associate Editor Katerina Michaelides, and Grant Meyer and two anonymous reviewers for their helpful comments that significantly improved the paper. All data are available upon request from the corresponding author.

References

- Allen, C. D., R. S. Anderson, R. B. Jass, J. L. Toney, and C. H. Baisan (2008), Paired charcoal and tree-ring records of high-frequency Holocene fire from two New Mexico bog sites, *Int. J. Wildland Fire*, *17*(1), 115–130.
- Anderson, R. S., R. B. Jass, J. L. Toney, C. D. Allen, L. M. Cisneros-Dozal, M. Hess, J. Heikooop, and J. Fessenden (2008), Development of the mixed conifer forest in northern New Mexico and its relationship to Holocene environmental change, *Quat. Res.*, *69*, 263–275, doi:10.1016/j.yqres.2007.12.002.
- Andrews, E. (1980), Effective and bankfull discharge in the Yampa River Basin, Colorado and Wyoming, *J. Hydrol.*, *46*, 311–330.
- Andrews, E. D., and J. M. Nankervis (1995), Effective discharge and the design of channel maintenance flows for gravel-bed rivers, in *Natural and Anthropogenic Influences in Fluvial Geomorphology*, *Monogr. Ser.*, vol. 89, pp. 151–164, AGU, Washington, D. C.
- Armour, J., P. J. Fawcett, and J. W. Geissman (2002), 15 k.y. paleoclimatic and glacial record from northern New Mexico, *Geology*, *30*(8), 723–726, doi:10.1130/0091-7613(2002)030<0723:KYPAGR>2.0.CO;2.
- Blagbrough, J. W. (1994), Late Wisconsin climatic inferences from rock glaciers in south-central and west-central New Mexico and east-central Arizona, *N. M. Geol.*, *16*, 65–71.
- Blakely, B. D., J. J. Coyle, and J. G. Steele (1957), *Soil—Yearbook of Agriculture*, pp. 308–314, U.S. Dept. Agriculture, U.S. Govt. Print. Off., Washington, D. C.
- Clark, M. L., C. A. Eddy-Miller, and M. A. Mast (2000), Environmental characteristics and water quality of hydrologic benchmark stations in the western United States, 1963–95, *U.S. Geol. Surv. Circ.*, *1173*, 115.
- Costa, J. E. (1984), Physical geomorphology of debris flows, in *Developments and Applications of Geomorphology*, edited by J. E. Costa and P. J. Fleisher, pp. 268–317, Springer, Berlin.
- Dewar, J. J. (2011), Fire history of montane grasslands and ecotones of the Valles Caldera, New Mexico, USA, Univ. of Arizona Master's thesis, 193 pp.
- DiBiase, R. A., K. X. Whipple, A. M. Heimsath, and W. B. Ouimet (2010), Landscape form and millennial erosion rates in the San Gabriel Mountains, CA, *Earth Planet. Sci. Lett.*, *289*, 134–144, doi:10.1016/j.epsl.2009.10.036.
- Eads, R. E., and R. B. Thomas (1983), Evaluation of a depth proportional intake device for automatic pumping samplers, *Water Resour. Bull.*, *19*(2), 289–292, doi:10.1111/j.1752-1688.1983.tb05328.x.
- Ferguson, R. I. (1986), River loads underestimated by rating curves, *Water Resour. Res.*, *22*, 74–76, doi:10.1029/WR022i001p00074.
- Ferguson, R. I., and T. A. Stott (1987), Forestry effects on suspended sediment and bedload yields in the Balquhiddie catchments, Central Scotland, *Trans. R. Soc. Edinburgh: Earth Sci.*, *78*, 379–384, doi:10.1017/S0263593300011317.
- Fitch, E. P., and G. Meyer (2013), Holocene fire, climate, and erosion in the Jemez Mountains, New Mexico, AGU, Fall Meeting 2013, Abstract GC24A-05.
- Fitch, E. P., and G. Meyer (2015), Temporal and spatial climatic controls on Holocene fire-related erosion and sedimentation, Jemez Mountains, New Mexico, *Quat. Res.*, *85*, 75–86, doi:10.1016/j.yqres.2015.11.008.
- Fowler, J. M. (1979), The interface of forestry and agriculture as nonpoint sources of suspended sediment: A national modeling approach, PhD dissertation, 244 pp., Iowa State Univ., Ames.
- Fowler, J. M., and E. O. Heady (1981), Suspended sediment production potential on undisturbed forest land, *J. Soil Water Conserv.*, *36*, 47–50.
- Goff, F., J. N. Gardner, S. L. Reneau, and C. J. Goff (2006a), Preliminary geologic map of the Redondo Peak Quadrangle, Sandoval County, New Mexico, Bureau of Geology and Mineral Resources Open-File Digital Geologic Map OF-GM 111.
- Goff, F., S. L. Reneau, C. J. Goff, J. N. Gardner, P. G. Drakos, and D. Katzman (2006b), Preliminary geologic map of the Valle San Antonio Quadrangle, Sandoval County, New Mexico, Bureau of Geology and Mineral Resources Open-File Digital Geologic Map OF-GM 132.
- Gosse, J. C., and F. M. Phillips (2001), Terrestrial in situ cosmogenic nuclides: Theory and application, *Quat. Sci. Rev.*, *20*, 1475–1560, doi:10.1016/S0277-3791(00)00171-2.
- Granger, D. E., J. W. Kirchner, and R. Finkel (1996), Spatially averaged long-term erosion rates measured from in situ-produced cosmogenic nuclides in alluvial sediment, *J. Geol.*, *104*(3), 249–257, doi:10.1130/L407.1.
- Grant, G. E., and A. L. Wolff (1991), Long-term patterns of sediment transport after timber harvest, western Cascade mountains, Oregon, USA, in *Sediment and Stream Water Quality in a Changing Environment: Trends and Explanation*, vol. 203, edited by E. N. Peters and E. D. Walling, pp. 31–40, IAHS Publ., Vienna.
- Istanbulluoglu, E., D. G. Tarboton, R. T. Pack, and C. Luce (2003), A sediment transport model for incision of gullies on steep topography, *Water Resour. Res.*, *39*(4), 1103, doi:10.1029/2002WR001467.
- Istanbulluoglu, E., D. G. Tarboton, R. T. Pack, and C. H. Luce (2004), Modeling of the interactions between forest vegetation, disturbances, and sediment yields, *J. Geophys. Res.*, *109*, F01009, doi:10.1029/2003JF000041.
- Kipfmüller, K. F., and W. L. Baker (2000), A fire history of a subalpine forest in south-eastern Wyoming, USA, *J. Biogeogr.*, *27*, 71–85, doi:10.1046/j.1365-2699.2000.00364.x.
- Kirchner, J. W., R. C. Finkel, C. S. Riebe, D. E. Granger, J. L. Clayton, J. G. King, and W. F. Megahan (2001), Mountain erosion over 10 yr, 10 k.y., and 10 m.y. time scales, *Geology*, *29*(7), 591–594, doi:10.1130/0091-7613(2001)029<0591:MEOYKY>2.0.
- Lal, D. (1991), Cosmic ray labeling of erosion surfaces: In situ nuclide production rates and erosion models, *Earth Planet. Sci. Lett.*, *104*, 424–439, doi:10.1016/0012-821x(91)90220-c.
- Li, Y. (2013), Determining topographic shielding from digital elevation models for cosmogenic nuclide analysis: A GIS approach and field validation, *J. Mt. Sci.*, *10*(3), 355–362, doi:10.1007/s11629-013-2564-1.
- Ma, Y., H. Q. Huang, J. Xu, G. J. Brierley, and Z. Yao (2010), Variability of effective discharge for suspended sediment transport in a large semi-arid river basin, *J. Hydrol.*, *388*, 357–369.
- Malmon, D. V., S. L. Reneau, D. Katzman, A. Lavine, and J. Lyman (2007), Suspended sediment transport in an ephemeral stream following wildfire, *J. Geophys. Res.*, *112*, F02006, doi:10.1029/2005JF000459.
- Margolis, E. Q., T. W. Swetnam, and C. D. Allen (2007), A stand-replacing fire history in upper montane forests of the southern Rocky Mountains, *Can. J. Forest Res.*, *37*(11), 2227–2241.
- Margolis, E. Q., T. W. Swetnam, and C. D. Allen (2011), Historical stand-replacing fire in upper montane forests of the Madran Sky Islands and Mogollon Plateau, southwestern USA, *Fire Ecol.*, *7*(3), 88–107.
- Meyer, G. A., S. G. Wells, and A. J. T. Jull (1995), Fire and alluvial chronology in Yellowstone National Park: Climatic and intrinsic controls on Holocene geomorphic processes, *Geol. Soc. Am. Bull.*, *107*(10), 1211–1230, doi:10.1130/0016-7606(1995)107<1211:FAACIY>2.3.CO;2.
- Meyer, G. A., J. L. Pierce, S. H. Wood, and A. J. T. Jull (2001), Fire, storms, and erosional events in the Idaho batholith, *Hydrol. Process.*, *15*(15), 3025–3038, doi:10.1002/hyp.389.
- Miller, J. D., H. D. Safford, M. Crimmins, and A. E. Thode (2009), Quantitative evidence for increasing forest fire severity in the Sierra Nevada and Southern Cascade Mountains, California and Nevada, USA, *Ecosystems*, *12*(1), 16–32, doi:10.1007/s10021-008-9201-9.

- Montgomery, D. R. (2007), Soil erosion and agricultural sustainability, *Proc. Natl. Acad. Sci. U.S.A.*, *104*, 13,268–13,272, doi:10.1073/pnas.
- Moody, J. A. (2012), An analytical method for predicting post-wildfire peak discharges, U.S. Geol. Surv. Sci. Invest. Rep. 2011–5236, U.S. Geol. Surv., Reston, Va., 36 p.
- Muldavin, E., and P. Tonne (2003), A vegetation survey and preliminary ecological assessment of Valles Caldera National Preserve, New Mexico, Report for Cooperative Agreement, 01CRAG0014, Univ. of New Mexico, N.M., 118 p.
- Nichols, M. H., J. J. Stone, and M. A. Nearing (2008), Sediment database, Walnut Gulch Experimental Watershed, Arizona, United States, *Water Resour. Res.*, *44*, W05S06, doi:10.1029/2006WR005682.
- Orem, C., and J. D. Pelletier (2015), Quantifying the time scale of elevated geomorphic response following wildfires using multi-temporal LiDAR data: An example from the Las Conchas fire, Jemez Mountains, New Mexico, *Geomorphology*, *232*, 224–238, doi:10.1016/j.geomorph.2015.01.006.
- Ott, R. L., and M. Longnecker (2001), *An Introduction to Statistical Methods and Data Analysis*, Texas A&M Univ., Duxbury Pacific Grove, Calif.
- Passalacqua, P., et al. (2015), Analyzing high resolution topography for advancing the understanding of mass and energy transfer through landscapes: A review, *Earth Sci. Rev.*, *148*, 174–193, doi:10.1016/j.earscirev.2015.05.012.
- Pelletier, J. D., and C. A. Orem (2014), How do sediment yields from post-wildfire debris-laden flows depend on terrain slope, soil burn severity class, and drainage basin area?, *Earth Surf. Process. Landforms*, *39*, 1822–1832, doi:10.1002/esp.3570.
- Phillips, E. H., F. Goff, P. R. Kyle, W. C. McIntosh, N. W. Dunbar, and J. N. Gardner (2007), The $^{40}\text{Ar}/^{39}\text{Ar}$ age constraints on the duration of resurgence at the Valles Caldera, New Mexico, *J. Geophys. Res.*, *112*, B08201, doi:10.1029/2006JB004511.
- Pierce, J., and G. Meyer (2008), Long-term fire history from alluvial fan sediments: The role of drought and climate variability, and implications for management of Rocky Mountain forests, *Int. J. Wildland Fire*, *17*, 84–95, doi:10.1071/WF07027.
- Pierce, J. L., G. A. Meyer, and A. J. T. Jull (2004), Fire-induced erosion and millennial-scale climate change in northern ponderose pine forests, *Nature*, *432*, 87–90, doi:10.1038/nature03058.
- Pimentel, D., E. C. Terhune, R. Dyson-Hudson, S. Rochereau, R. Samis, E. A. Smith, D. Denman, D. Reifschneider, and M. Shepard (1976), Land degradation: Effects on food and energy resources, *Science*, *194*, 149–155, doi:10.1126/science.194.4261.149.
- Riebe, C. S., J. W. Kirchner, D. E. Granger, and R. C. Finkel (2000), Erosional equilibrium and disequilibrium in the Sierra Nevada inferred from cosmogenic ^{26}Al and ^{10}Be alluvial sediment, *Geology*, *28*(9), 803–806, doi:10.1130/0091-7613(2000)28<803:EEADIT>2.0.CO;2.
- Riley, K., J. Pierce, and G. A. Meyer (2015), Vegetative and climatic controls on Holocene wildfire and erosion recorded in alluvial fans of the Middle Fork Salmon River, Idaho, *Holocene*, doi:10.1177/0959683615571424.
- Santi, P., and L. Morandi (2013), Comparison of debris-flow volume from burned and unburned areas, *Landslides*, *10*(6), 757–769, doi:10.1007/s10346-012-0354-4.
- Shakesby, R. A., and S. H. Doerr (2006), Wildfire as a hydrological and geomorphological agent, *Earth Sci. Rev.*, *74*, 269–307, doi:10.1016/j.earscirev.2005.10.006.
- Sibold, J. S., T. T. Veblen, and M. E. Gonzalez (2006), Spatial and temporal variation in historic fire regimes in subalpine forests across the Colorado Front Range in Rocky Mountain National Park, Colorado, USA, *J. Biogeogr.*, *32*, 631–647, doi:10.1111/j.1365-2699.2005.01404.x.
- Stone, J. O. (2000), Air pressure and cosmogenic isotope production, *J. Geophys. Res.*, *105*(B10), 23,753–23,759, doi:10.1029/2000JB900181.
- Swanson, F. J. (1981), Fire and geomorphic processes, fire regimes and ecosystem properties, in *USDA Forest Service General Technical Report WO-26*, edited by H. A. Mooney et al., pp. 401–420, USDA, Washington, D. C.
- Touchan, R., C. D. Allen, and T. W. Swetnam (1996), *Fire Effects in Southwestern Forests: Proceedings of the Second La Mesa Fire Symposium*. Fort Collins, CO: *USDA Forest Service General Technical Report RM-GTR-286*, edited by C. D. Allen, pp. 33–46, U.S. Department of Agriculture, Rocky Mountain Forest and Range Experiment Station, Fort Collins, Colo.
- Toyoda, S., F. Goff, S. Ikeda, and M. Ikeya (1995), ESR dating of quartz phenocrysts in the El Cajete and Battleship Rock Members of the Valles Rhyolite, Valles Caldera, New Mexico, *J. Volcanol. Geotherm. Res.*, *67*, 29–40, doi:10.1016/0377-0273(94)00093-V.
- U.S. Department of Agriculture (2008), Soil Survey of Sandoval County Area, New Mexico, Parts of Los Alamos, Sandoval, and Rio Arriba Counties, 924 p., digital document. [Available at http://www.nrcs.usda.gov/Internet/FSE_MANUSCRIPTS/new_mexico/NM656/0/Sandoval%20NM.pdf.]
- Veblen, T. T., K. S. Hadley, E. M. Nel, T. Kitzberger, M. Reid, and R. Villalba (1994), Disturbance regime and disturbance interactions in a Rocky Mountain subalpine forest, *J. Ecol.*, *82*(1), 125–135, doi:10.2307/2261392.
- von Blanckenburg, F. (2005), The control mechanisms of erosion and weathering at basin scale from cosmogenic nuclides in river sediment, *Earth Planet. Sci. Lett.*, *237*, 462–479, doi:10.1016/j.epsl.2005.06.030.
- Wagenbrenner, J. W., and P. R. Robichaud (2014), Post-fire bedload sediment delivery across spatial scales in the interior western United States, *Earth Surf. Process. Landf.*, *39*, 865–876, doi:10.1002/esp.3488.
- Walling, D. E. (1974), Suspended sediment and solute yields from a small catchment prior to urbanization, in *Fluvial Processes in Instrumented Watersheds, Spec. Publ.*, vol. 6, edited by K. J. Gregory and D. E. Walling, pp. 169–192, Institute of British Geographers, London.
- Weppner, K. N., J. L. Pierce, and J. L. Betancourt (2003), Holocene fire occurrence and alluvial responses at the leading edge of pinyon-juniper migration in the Northern Great Basin, USA, *Quat. Res.*, *80*(2), 143–157, doi:10.1016/j.yqres.2013.06.004.
- Westerling, A. L., H. G. Hidalgo, D. R. Cayan, and T. W. Swetnam (2006), Warming and earlier spring increase western U.S. forest wildfire activity, *Science*, *313*, 940–943, doi:10.1126/science.1128834.
- Williams, A. P., et al. (2013), Temperature as a potent driver of regional forest drought stress and tree mortality, *Nat. Clim. Change*, *3*, 292–297, doi:10.1038/nclimate1693.
- Wolman, M. G., and R. Gerson (1978), Relative scales of time and effectiveness of climate in watershed geology, *Earth Surf. Process.*, *3*, 189–208.
- Wolman, M. G., and J. P. Miller (1960), Magnitude and frequency of forces in geomorphic processes, *J. Geol.*, *68*, 54–74, doi:10.1086/626637.
- Zapata-Rios, X., P. D. Brooks, P. A. Troch, J. McIntosh, and Q. Guo (2015), Influence of terrain aspect on water partitioning, vegetation structure and vegetation greening in high-elevation catchments in northern New Mexico, *Ecohydrology*, doi:10.1002/eco.1674.